

that the yield of matrix-trapped excess electrons in D₂O is larger than in H₂O and concluded that D₂O is less efficient in the initial electron localization (to yield the solvated electron) than H₂O. The reason for this difference is ascribed to the lower vibrational frequency of D₂O. Therefore D₂O is more prone to autodetachment, and this process can compete more favorably with the transfer of the excess energy (electron affinity) to the lattice, which is required for prelocalization.

Conclusion

Our experiments demonstrate that efficient mechanisms exist for the trapping of low energy electrons at cold, preexisting water clusters in the size range $n \leq 12$. Thus, the initial localization of an electron at a cluster does not require large configurational fluctuations or molecular reorientation. Similar mechanisms seem to exist for other systems as well. The vertical electron affinity of CO₂, e.g., is strongly negative, because the geometry of CO₂⁻ in its ground-state deviates appreciably from the geometry of neutral CO₂. Nevertheless, a CO₂ cluster anion can be formed efficiently by attachment of near-0-eV electrons.

Our results do not, however, answer the question whether a solvated electron represents the ground state of a cluster anion comprised of as few as 12 water molecules.

Note Added in Proof. From a recent molecular dynamics simulation of electrons in liquid water⁶¹ it has been concluded that the concentration of preexisting deep traps is much higher than thought previously. Thus, electron solvation might proceed very rapidly, without significant structural relaxation.

Acknowledgment. It is a pleasure to thank K. Bowen, H. Haberland, and T. D. Märk for stimulating discussions, and C. E. Klots for critical comments on the manuscript. This work was financially supported by the Deutsche Forschungsgemeinschaft.

Registry No. H₂O, 7732-18-5.

(59) Krohn, C. E.; Antoniewicz, P. R.; Thompson, J. C. *Surf. Sci.* **1980**, 101, 241.

(60) Kestner, N. R., private communication.

(61) Schnitker, J.; Rossky, P. J.; Kenney-Wallace, G. A. *J. Chem. Phys.* **1986**, 85, 2986. Schnitker, J.; Rossky, P. J., preprint.

Generalized Valence Bond Studies of Metallic Bonding: Naked Clusters and Applications to Bulk Metals

Mark H. McAdon[†] and William A. Goddard III*

Arthur Amos Noyes Laboratory of Chemical Physics,[‡] California Institute of Technology, Pasadena, California 91125 (Received: June 17, 1986)

Using the generalized valence bond (GVB) method, we have examined the bonding in numerous small clusters of Li atoms (Li_n and Li_n⁺, $n \leq 13$). Our conclusion is that the optimum bonding involves interstitially localized *singly occupied* orbitals, e.g., (1) bond-centered orbitals for one-dimensional clusters (e.g., rings such as Li₄, Li₆, Li₈, and Li₁₀ and linear chains such as Li₃⁺, Cu₃⁺, Li₈⁺, Li₈⁻, and Li₁₃⁺), (2) equilateral-triangle-centered orbitals for planar close-packed clusters (e.g., Li₁₀, Li₁₂⁴⁺, and Li₁₃⁺), and (3) tetrahedron-centered orbitals for three-dimensional clusters (examples here include three high-symmetry [icosahedral (I_h), face-centered cubic (fcc), and hexagonal close-packed (hcp)] Li₁₃⁺ structures and three low symmetry [γ -brass-like] Li₁₃⁺ structures. Of the three high symmetry Li₁₃⁺ clusters, I_h has the lowest energy while total energies for fcc and hcp are 0.26 and 0.56 eV higher, respectively. GVB wave functions for these three clusters suggest a set of rules predicting structures even more stable than the icosahedron. These lower energy structures [denoted as OPTET (optimum tetrahedral)] maximize the number of tetrahedra under the restrictions of the rules (e.g. minimizing the number of occupied tetrahedra sharing corners) and lead to relatively low symmetry, e.g. C_{2v}, C_s. These OPTET clusters coincide with truncations of the γ -brass structure. The lowest energy Li₁₃⁺ OPTET cluster [γ -(4,4,5), C_{2v}] has a total energy 0.58 eV lower than that of the icosahedron. Suggestions are given on the relevance of these results for stability and reactivity of small clusters and on the extension of these ideas to infinite systems.

I. Introduction

The valence bond (VB) principles of structural chemistry,¹ based on spin pairing of hybridized atomic orbitals on various atoms, lead to excellent rationalization of the geometries and bonding for nonmetallic molecules and solids; e.g., bulk Si and Ge are tetrahedrally coordinated, Se and Te have helical chains in their solid forms, the As₄ molecule has a tetrahedron structure with a single bond along each edge, etc. These simple VB ideas of nonmetallic systems have been confirmed by ab initio generalized valence bond (GVB) calculations² that lead directly to localized spin-paired atomic orbitals corresponding to various bond pairs. Valence bond principles have also proven valuable in understanding defects and surface reconstruction in nonmetallic solids, e.g. the Si vacancy³ and the GaAs(110) surface.⁴

For metallic systems, there has not been an analogous set of simple principles to predict a priori the optimum geometries and structures of clusters, defects, or interfaces. In order to lay the

foundation for developing chemical concepts for *metallic* systems, we have employed GVB approaches to examine the bonding in various one-dimensional (1D),⁵ two-dimensional (2D), and three-dimensional (3D) clusters of Li atoms. The results of this study have led directly to a new *generalized valence bond model of metallic bonding*^{6,7} based on electrons localized in interstitial regions such as bond midpoints (1D clusters), triangular faces (2D clusters), and tetrahedral hollows (3D clusters). This model is

(1) Pauling, L. *The Nature of the Chemical Bond*, 3rd ed.; Cornell University Press: Ithaca, New York, 1960.

(2) Goddard III, W. A.; Dunning, Jr., T. H.; Hunt, W. J.; Hay, P. J. *Acc. Chem. Res.* **1973**, 6, 368. Goddard III, W. A.; Harding, L. B. *Annu. Rev. Phys. Chem.* **1978**, 29, 363.

(3) Surratt, G. T.; Goddard III, W. A. *Solid State Commun.* **1977**, 22, 413. *Phys. Rev. B* **1978**, 18, 2831.

(4) Barton, J. J.; Goddard III, W. A.; McGill, T. C. *J. Vac. Sci. Technol.* **1979**, 16, 1178. Swarts, C. A.; McGill, T. C.; Goddard III, W. A. *Surf. Sci.* **1981**, 110, 400.

(5) McAdon, M. H.; Goddard III, W. A., unpublished results.

(6) McAdon, M. H.; Goddard III, W. A. *Phys. Rev. Lett.* **1985**, 55, 2563.

(7) McAdon, M. H.; Goddard III, W. A. *J. Non-Cryst. Solids* **1985**, 75, 149.

[†]A.R.C.S. Foundation Predoctoral Fellow, 1985-1986.

[‡]Contribution No. 7413.

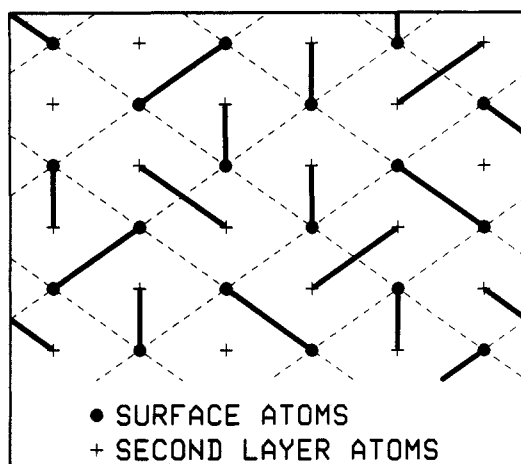


Figure 1. The simple VB description of metals [for the body-centered cubic Li(110) surface]. Thin lines connect nearest-neighbor atoms at the surface. Thick lines represent two-center, two-electron covalent bonds for one of numerous simple VB resonance structures.

summarized by a simple set of rules (see section IV) based on singly occupied valence electron orbitals centered in tetrahedral hollows.

We have used these rules to predict the low-energy Li_{13}^+ isomers [denoted as OPTET (optimum tetrahedral)]. GVB calculations confirm that these OPTET structures are significantly more stable than the traditional high-symmetry 13-atom structures. The high-symmetry icosahedron, fcc-like and hcp-like structures have total energies higher than the best OPTET cluster [OPTET(I)] by 0.58, 0.84, and 1.14 eV, respectively. These OPTET isomers all have local fivefold symmetry axes which result from the efficient packing of tetrahedra. Two of the three OPTET clusters (I and II) also clearly coincide with truncations of the γ -brass structure. Thus, we also refer to these two OPTET isomers as γ -brass clusters. The correspondence of the third structure to a truncation of γ -brass is rather subtle; however, OPTET(III) is more clearly based on a modification of the icosahedron.

We believe that these principles should prove useful in rationalizing and predicting the geometric and electronic structures of such localized phenomena as defects, interfaces, and chemisorbed species for metallic systems. We have applied the principles to bulk close-packed metals and find that they are consistent with known solid solubilities and alloy structures. The OPTET clusters could also form a basis for certain classes of amorphous metals,⁷ since the exact fivefold symmetry axes favored by OPTET cannot lead to solids with long-range (periodic) order. Thus the principles presented here may lead to new insights regarding how local structure and alloying may control formation of amorphous metallic systems.

Section II presents further background material. Results for the various clusters are given in section III and details of the calculations are given in the Appendix. Extension of the rules to bulk metals is given in section IV.

II. The GVB Model

The simple VB description of metals^{1,8} involves two-center, two-electron covalent bonds between adjacent atoms (Figure 1). Since metallic systems have too few electrons and are too highly coordinated to simultaneously allow one bond between each pair of adjacent atoms, the simple VB description involves numerous equivalent such bonding or resonance structures superimposed to describe the many-electron (total) wave function.^{1,8,9} This simple extension of the VB concepts so useful for nonmetallic systems has not led to a very useful description of metallic systems.

A hint of the problem is seen from a simple estimate of the cohesive energy of lithium. The total cohesive energy or atom-

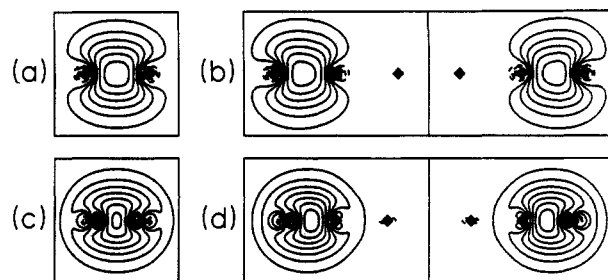


Figure 2. The optimum GVB valence orbitals for (a) Li_2^+ , (b) linear Li_3^+ , (c) Cu_2^+ , and (d) linear Cu_3^+ . Each orbital contains one electron. Two separate orbitals are shown for Li_3^+ (b, 0.21 overlap) and two separate orbitals are shown for Cu_3^+ (d, 0.40 overlap). The orbitals for Li_2^+ and linear Li_3^+ are shown for $R = 3.1 \text{ \AA}$. The orbitals for Cu_2^+ and linear Cu_3^+ are shown for $R = 2.556 \text{ \AA}$. All cases are drawn to equal scale (each box shows 6.2 \AA width). In Figures 2 and 3 and in similar figures that follow, solid contours denote positive orbital amplitudes and dashed contours represent negative orbital amplitudes (for normalized singly occupied orbitals). Unless otherwise noted, the contours represent orbital amplitude increments of 0.015 au and squares mark the atomic positions.

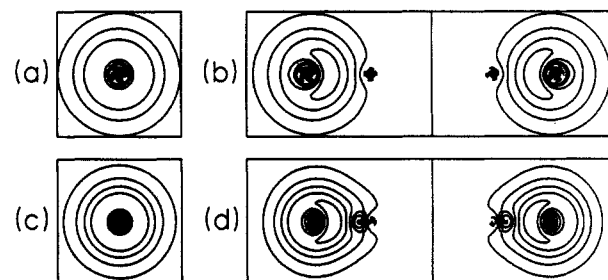
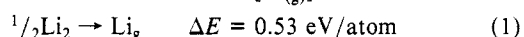
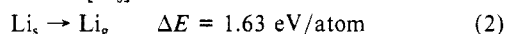


Figure 3. The optimum GVB valence orbitals for (a) Li atom, (b) Li_2 , (c) Cu atom, and (d) Cu_2 . Each orbital contains one electron. Two separate orbitals are shown for Li_2 (b, 0.58 overlap) and two separate orbitals are shown for Cu_2 (d, 0.62 overlap). The scales (and bond lengths for the dimers) are consistent with Figure 2.

ization energy of lithium would be estimated by adding all of the Li-Li bond energies to obtain the total bond energy for one bonding structure (resonance configuration) and then adding the additional stabilization (resonance energy) due to the interaction of all the resonance structures.⁹ The effective bond energy for each Li-Li bond can be estimated from the dissociation energy¹⁰ of the Li_2 molecule into free atoms [$\text{Li}_{(\text{g})}$]



This can be compared with the experimental bulk atomization energy¹¹ of the solid [Li_3]



Thus, in order to explain the cohesive energy of the solid, the resonance energy would have to be 1.10 eV/atom, or over twice the intrinsic bond energy! Such a large resonance energy is clearly implausible.

An alternative to such VB descriptions is suggested by the following observations.

(1) The bond strength for the one-electron bond (Figure 2a) of the Li_2^+ molecule (1.30 eV^{12,13} or 1.30 eV per valence electron) is 80% of the cohesive energy (per bonding electron) for Li metal [and a factor of 2.45 greater than the bond strength (per bonding electron) of Li_2].

(10) Verma, K. K.; Koch, M. E.; Stwalley, W. C. *J. Chem. Phys.* 1983, 78, 3614. In order to compare bond energies for the bulk metal and for Li_2 , the total bond energy of Li_2 , 1.06 eV/molecule ($\text{Li}_2 \rightarrow 2\text{Li}$) is divided by 2, obtaining the per atom bond energy, 0.53 eV/atom.

(11) Hultgren, R.; Desai, P. D.; Hawkins, D. T.; Gleiser, M.; Kelley, K. K.; Wagman, D. D. *Selected Values of the Thermodynamic Properties of the Elements*; American Society for Metals: Metals Park, OH, 1973.

(12) Konowalow, D. D.; Rosenkrantz, M. E. *Chem. Phys. Lett.* 1979, 61, 489.

(13) Bernheim, R. A.; Gold, L. P.; Tipton, T. J. *J. Chem. Phys.* 1983, 78, 3635.

(8) Pauling, L. *Proc. R. Soc. London, Ser. A* 1949, 196, 343.

(9) Feynman, R. P.; Leighton, R. B.; Sands, M. *The Feynman Lectures on Physics*; Addison-Wesley: Reading, MA, 1965.

(2) The bonding in linear Li_3^+ involves two singly occupied orbitals,¹⁴ one localized at each Li-Li bond midpoint (Figure 2b) with an overlap (0.214) much smaller than that of normal two-electron bonds. These singly occupied bond orbitals are very similar to the optimum orbital of Li_2^+ (Figure 2a), but quite different from the 2s orbital of Li atom (Figure 3a) and the optimum orbitals of Li_2 (Figure 3b) on which the simple VB model is based.

Based on these observations,¹⁵ we suspected that the best simple description of extended Li systems is in terms of *singly occupied orbitals localized interstitially*. This led to the *generalized valence bond* studies reported herein on one-, two-, and three-dimensional lithium clusters that do indeed indicate that the bonding involves singly occupied orbitals localized in bond midpoints, triangular faces, and tetrahedral hollows. In addition, the valence orbitals for Cu atom, Cu_2 (Figure 3c-d), Cu_2^+ , and linear Cu_3^+ (Figure 2c-d) are very similar to those for Li atom, Li_2 (Figure 3a-b), Li_2^+ , and linear Li_3^+ (Figure 2a-b). [For these lithium systems, the optimum GVB orbitals are plotted for a bond length (R) of 3.10 Å, which is in the range of the experimental bond lengths (or nearest-neighbor distances) for Li_2^+ (3.113 ± 0.013 Å),¹³ the close-packed form of Li_8 (3.105 Å at 78 K)¹⁶ and the body-centered-cubic form of Li_8 (3.016 Å at 78 K).¹⁶ For the Cu systems, $R = 2.556$ Å was chosen which corresponds to the value for face-centered-cubic Cu_8 at 298 K. For Cu, we used an effective potential¹⁷ while the Li calculations are all-electron ab initio (see the Appendix).] The similarity of the valence orbitals for the Cu and Li systems suggests that the results presented in this paper for lithium should also apply to the noble metals and the valence sp electrons of transition metals.

III. Results

In the generalized valence bond (GVB) description, each valence electron is allowed to be in a different orbital, where the orbitals are allowed full freedom with respect to localization, delocalization, hybridization, and overlap. The form of the GVB wave function^{2,18} ensures that the Pauli principle and proper spin symmetry are obtained independent of the orbitals. Thus, GVB differs from Hartree-Fock type wave functions, where the proper spin symmetry is obtained only when down-spin orbitals and up-spin orbitals coincide. Details of the GVB wave functions are given in Appendix A. In this section, it is sufficient to understand that the GVB wave function provides the optimal one-electron picture.^{2,18}

The orbitals are calculated self-consistently and the total wave function is thought of in terms of N electrons, each electron in its own optimum orbital (moving in the field due to the remaining $N - 1$ electrons in their optimum orbitals). Thus, we use the terms electron and orbital interchangeably. In general, we find that the GVB orbitals tend to be well localized, leading to a natural classification in terms of "bulk" orbitals or "surface" orbitals. We find that the bulk orbitals tend to be centered in bond midpoints, triangular faces, and tetrahedral hollows for 1D, 2D, and 3D structures, respectively. Surface orbitals tend to be centered in surface triangular faces or bond midpoints for 3D structures, and in edge bond midpoints for 2D structures. For the linear chain clusters (1D), the surface orbitals tend to be at the ends of the chain, polarized away from the chain toward the vacuum.

In this paper we focus upon clusters of Li atoms. However, similar calculations on other alkali metals (Na, K, Rb, Cs, Fr) and on noble metals (Cu, Ag, Au) are expected to yield very similar results.

(14) Kahn, L. R.; Goddard III, W. A. *J. Chem. Phys.* 1972, 56, 2685.

(15) An early (unpublished) test of these ideas by T. H. Upton and W. A. Goddard III showed that the ground state of hexagonal Li_6 involves one valence electron localized at each bond midpoint.

(16) Donohue, J. *The Structure of the Elements*; Wiley: New York, 1974.

(17) Hay, P. J.; Wadt, W. R. *J. Chem. Phys.* 1985, 82, 270. The effective potential for Cu included the effects of the [Ar] shell, leaving eleven electrons to be treated explicitly ($3d^{10}4s^1$). It is fairly obvious that the second coefficient for the d-f potential should be -0.4621680 rather than the listed value of $+0.4621680$, and with this change we were able to reproduce the results listed by Hay and Wadt in Tables XIII-XIV of their paper.

(18) Goddard III, W. A. *Int. J. Quantum Chem.* 1970, IIIS, 593. Goddard III, W. A.; Ladner, R. C. *J. Chem. Phys.* 1969, 51, 1073.

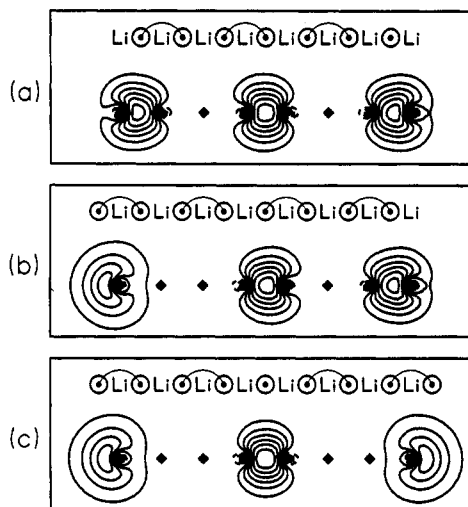


Figure 4. The GVB description of the (a) Li_8^+ , (b) Li_8 , and (c) Li_8^- chain clusters ($R = 3.1$ Å). The schematic diagrams show all of the singly occupied GVB orbitals with the spin coupling for the principal resonance structure represented by connected dots. In each case orbitals at the middle and both ends are shown in contour plots. Overlaps for adjacent spin-paired bond-centered orbitals are ≈ 0.34 . Overlaps for diffuse surface orbitals spin paired to adjacent bond orbitals are ≈ 0.52 .

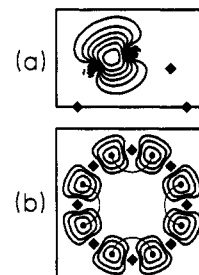


Figure 5. The GVB orbitals for one of the two primary resonance structures of the Li_8 ring cluster ($R = 3.1$ Å). Squares mark the atomic positions and dots joined by thin lines represent the electrons and spin coupling. (a) One singly occupied GVB orbital. (b) Contours ≥ 0.045 au for all eight GVB orbitals. Spin-paired orbitals have overlaps of 0.36.

A. One-Dimensional Clusters. The valence electronic structure of the infinitely long 1D Li chain [$\text{Li}_{(1D)}$] involves one electron localized at each bond midpoint, each electron forming a one-electron bond as in Li_2^+ . This is shown for the Li_8 chain (Figure 4) and for the Li_8 ring (Figure 5), where the adjacent atom internuclear separation is $R = 3.1$ Å [near the equilibrium bond distance of $R_e = 3.14$ Å⁵ for $\text{Li}_{(1D)}$]. The Li_8^+ , Li_8 , and Li_8^- chains have seven singly occupied bond orbitals in common, one centered at each of the seven bond midpoints, and zero, one, or two singly occupied "surface" orbitals. Each of the seven bond orbitals contains one electron and is very similar to the bond orbitals of Li_2^+ or linear Li_3^+ . For the Li_8 ring, all eight valence electrons occupy bond midpoints.

In the lowest energy (primary) configurations, adjacent singly occupied orbitals are spin-paired [leading to two equivalent resonance structures for $\text{Li}_{(1D)}$]. The overlap between paired orbitals is small (≈ 0.34 for adjacent bond orbitals and ≈ 0.52 for a surface orbital paired to a bond orbital), whereas normal two-electron bonds have large overlaps of 0.7 to 0.8; thus, the bonding is dominated by the one-electron bonds, with two-electron spin-coupling effects somewhat less important.⁵ The lowest energy many-electron states are all low spin. Nevertheless, higher spin states (including states with adjacent orbitals high-spin coupled) involve similar orbitals and also lead to strong bonding. [Indeed, even the maximum spin state (e.g., spin $S = 4$ for the Li_8 ring) is bound strongly with respect to the separated atoms limit¹⁵.]

The orbitals in Figures 4 and 5 were optimized for the lowest energy resonance configuration (in some cases the orbitals are optimized for one of two equivalent lowest energy configurations). The Li_8^+ chain has one unpaired electron, leading to four primary

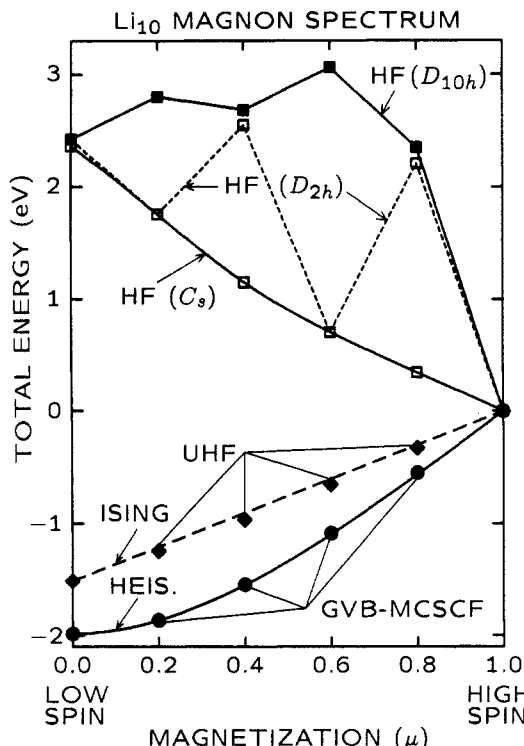


Figure 6. The total energy of Li_{10} ($R = 3.1 \text{ \AA}$) as a function of magnetization for HF, UHF, and GVB wave functions. The symmetry restrictions imposed on the HF orbitals are indicated in parentheses. Lines connecting the HF energies serve as a guide to the eye. The low-spin and high-spin states are fit to an Ising model for UHF (dashed line) and to a Heisenberg model for GVB (solid line). The root mean square errors for the fits of the Ising and Heisenberg models to the calculated energies of the four intermediate spin states are 0.044 and 0.010 eV for UHF and GVB, respectively.

resonance structures (one for each alternate bond midpoint), of which the two configurations lowest in energy have the unpaired electron at the bond midpoint adjacent to one of the surface atoms (see Figure 4a). The Li_8 chain has all electrons spin paired, but it leads to one surface orbital that can localize on either end of the chain, leading to two equivalent primary resonance structures (see Figure 4b). The unpaired electron of Li_8^- leads to five primary resonance configurations (see Figure 4c). Of these five configurations, the two configurations with one unpaired surface electron are substantially higher in total energy (≈ 0.25 eV) than the three configurations with one unpaired bond electron. This is because the overlap for a surface orbital paired to an adjacent bond orbital is $\approx 53\%$ larger than the overlap between two adjacent spin-paired bond orbitals. The Li_8 ring (Figure 5) has two equivalent primary resonance configurations [as does $\text{Li}_{(1D)}$]. The full GVB wave function for each of these four systems is dominated by the primary spin couplings, but this wave function allows a full optimization of the spin coupling and thus includes resonance configurations where nonadjacent orbitals are spin paired (for the low-spin Li_8 ring, there are a total of 14 resonance configurations). This is analogous to the VB description of benzene, involving the two Kekulé (primary) and three Dewar (secondary) resonance structures.¹ In the full GVB wave function, the orbitals and spin coupling are optimized simultaneously, leading to orbitals that are similar to (but not identical with) those shown in Figures 4 and 5; e.g., the single-particle full GVB orbitals for the Li_8 ring are localized exactly in the center of the bond midpoints and have equal overlaps with each of the two adjacent orbitals, leading to a fully symmetrical (D_{8h}) description.

B. Electron Correlation Effects. At this point it is important to discuss the effects of electron correlation in describing the bonding in naked metal clusters. We shall illustrate these electron correlation effects with results for the magnon spectrum (spectrum of excited spin states) of the symmetrical Li_{10} ring calculated with the restricted Hartree-Fock (HF), unrestricted Hartree-Fock

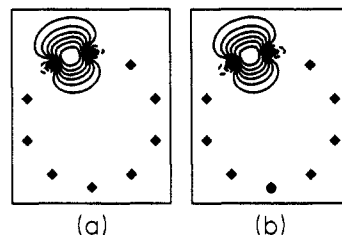


Figure 7. The Wannier orbital (ω_i) for the (a) high-spin state and (b) low-spin state of the Li_{10} ring. The scale and bond length ($R = 3.1 \text{ \AA}$) are consistent with Figures 4 and 5. In each case, the Wannier orbital is obtained from a Fourier transformation of ten D_{10h} symmetry orbitals and orbitals $\omega_2, \omega_3, \dots, \omega_{10}$ are obtained by rotating ω_1 .

(UHF), and generalized valence bond (GVB) wave functions. The energy of Li_{10} as a function of magnetization

$$\mu = \frac{2S}{n} \quad (3)$$

($n = 10$) is shown in Figure 6 for various wave functions (Ψ), where S is the eigenvalue (or spin quantum number) of the total spin operator (\hat{S}^2)

$$\hat{S}^2 \Psi_{n,S} = S(S+1)\hbar^2 \Psi_{n,S} \quad (4)$$

e.g., $S = 0$, singlet; $S = 1$, triplet, etc. A thorough discussion of the results of these calculations will be presented elsewhere;⁵ here, we shall simply touch upon the highlights. The general forms of these wave functions are discussed in greater detail in the Appendix.

The HF, UHF, and GVB wave functions are all identical for valence electron total high-spin ($\mu = 1$) states. Here, the optimum canonical valence orbitals are consistent with D_{10h} symmetry; i.e., they are what is commonly referred to as molecular orbitals (MO). The valence electron configuration of the lowest energy high-spin state of Li_{10} is $a_{1g}(\uparrow)e_{1u}(\uparrow\downarrow)e_{2g}(\uparrow\downarrow)e_{3u}(\uparrow\downarrow)e_{4g}(\uparrow\downarrow)b_{2u}(\uparrow)$ where all valence orbitals are σ and each electron is up-spin (\uparrow or α). This leads to an overall (many-electron) $^{11}\text{B}_{2u}$ state. The a_{1g} orbital has zero radial nodes ($m = 0$), the doubly degenerate $e_{m(g,u)}$ orbitals have m radial nodes, and the b_{2u} orbital has five radial nodes ($m = 5$). As expected, the MO one-electron energies increase roughly as m^2 , where m is the number of radial nodes. The $^{11}\text{B}_{2u}$ state of Li_{10} is strongly bound, with a total bond energy of 2.63 eV with respect to separated atoms. Extrapolating the results for various Li_n rings and chains to infinite n leads to $\text{Li}_{(1D)}$ where the lowest energy high-spin state is bound with respect to separated Li atoms by 0.29 eV/atom.⁵

The bonding in high-spin Li_{10} is due to high-spin coupled one-electron bond orbitals. Each MO in this wave function is composed of linear combinations of the ten localized bond-centered functions, one of which is shown in Figure 7a. Clearly, the orbital obtained from the high-spin state shown in Figure 7a is quite similar to the orbitals obtained from low-spin states shown in Figures 4 and 5. The Li 2p atomic functions (f_{2p}) are of vital importance in forming these one-electron bonds. The Li 2p functions can be split into three groups: $p\pi_\perp$ having their nodes in the plane of the ring, $p\pi_\parallel$ pointing radially outward from the ring (and becoming π orbitals in the limit as $n \rightarrow \infty$), and $p\sigma$, tangent to the ring and pointing at adjacent atoms. Each localized bond orbital (ω_i) as shown in Figure 7a would be referred to in the solid-state literature as a *Wannier orbital*¹⁹ and for Li_{10} the ω_i are composed of roughly half 2s character and roughly half 2p σ character, e.g.

$$\omega_i \approx f_{2s,a} + f_{2s,b} + f_{2p\sigma,a} - f_{2p\sigma,b} \quad (5)$$

where a and b signify two adjacent centers (recall that the bonding combination of 2p σ orbitals is out-of-phase). The ω_i also contain contributions due to 2s and 2p orbitals on nonadjacent atoms, but these contributions are quite small. The 2p σ orbitals are necessary to maintain the orthogonality of the adjacent high-spin orbitals,

e.g., the combinations $f_{2s,a} + f_{2p,a}$ and $f_{2s,a} - f_{2p,a}$ are orthogonal. Hence the a_{1g} orbital is simply the plus or bonding combination of all ten localized bond-centered orbitals and has no 2p character since the 2p coefficients of the ω_i are out-of-phase. Likewise, the b_{2u} orbital is derived from the antibonding combination of the ten localized bond-centered orbitals and has no 2s character since the 2s coefficients of the ω_i are in-phase.

The b_{2u} orbital is crucial to the bonding of the high-spin Li_{10} ring. The $^{11}\text{B}_{1u}$ excited high-spin state of the Li_{10} ring obtained by the elementary excitation $b_{1u} \leftarrow b_{2u}$ is totally repulsive at the HF level for all internuclear separations. Both the b_{1u} and b_{2u} orbitals are σ with respect to the plane of the ring and have five radial nodes ($m = 5$). However, the b_{1u} orbital is composed of the antibonding combination of 2s functions while the b_{2u} orbital is composed of the bonding combination of 2p σ functions. It is important to note here that theories such as the jellium model²⁰ and the Hückel model²¹ would fail in distinguishing between the b_{1u} and b_{2u} orbitals (and hence the $^{11}\text{B}_{1u}$ and $^{11}\text{B}_{2u}$ states).

Often single-determinant wave functions are used to describe the electronic states of extended systems. As discussed below, there are two general approaches: (1) UHF in which no restrictions are made upon the orbitals, often leading to total (many-electron) wave functions that are *not* eigenfunctions of \hat{S}^2 (and often do not have the proper spatial symmetry), and (2) HF in which spin and/or spatial restrictions are made in order to ensure that the total wave function has the correct spin and/or spatial symmetry. Although all methods (GVB, HF, UHF) are equivalent for the high-spin case, we find that neither UHF nor HF gives a correct description for other spin states.

The first point to emphasize for HF (and UHF) is that the optimum canonical orbitals are *not* always consistent with the symmetry of the molecule.

For all spins of Li_{10} other than $S = 5$, HF energies calculated with symmetry-adapted orbitals [orbitals optimized under the *restriction* that they transform according to the irreducible representations of D_{10h}] are significantly higher than those with the optimum orbitals (of C_s symmetry), as shown in Figure 6. Upon reducing the symmetry restriction to D_{2h} (or C_i), half of the spin states are still higher in energy than the results using C_s symmetry. This phenomenon of symmetry breaking is often described for bulk systems in terms of *charge density waves*^{22,23} (HF) or *spin density waves* (UHF) and for Li_{10} derives from a fundamental inconsistency in the use of single Slater determinant wave functions. A single determinant wave function containing doubly occupied orbitals forces ionic character into the wave function, which is in turn deleterious to the energy. For Li_{10} , the fraction of ionic character in the HF wave function decreases (and hence the total energy decreases) if the orbitals are allowed to localize even though this lowers the symmetry.⁵ Allowing for localization, the amount of ionic character (and thus the total energy) of the HF wave function increases monotonically with decreasing magnetization.

The UHF wave function avoids doubly occupied orbitals (and thus avoids ionic character), but, in the process, the orbitals tend to localize (i.e., break symmetry) resulting in spin density waves for all states of Li_{10} other than the $\mu = 1$ state. The UHF wave function is an eigenfunction of the spin projection operator (\hat{S}_z)

$$\hat{S}_z \Psi_n^{\text{UHF}}(M_S) = M_S \hbar \Psi_n^{\text{UHF}}(M_S) \quad (6)$$

where M_S is simply the half difference between the number of up-spin (α) and the number of down-spin (β) electrons. The UHF wave function with spin projection M_S contains a mixture of spins from $S = |M_S|$ to $S = n/2$ and thus is not an eigenfunction of the \hat{S}^2 operator (4) [we follow the standard convention for UHF

(20) Cleland, A. N.; Cohen, M. L. *Solid State Commun.* **1985**, *55*, 35. Clemenger, K. *Phys. Rev. B* **1985**, *32*, 1359.

(21) Wang, Y.; George, T. F.; Lindsay, D. M.; Beri, A. C.; unpublished results. Lindsay, D. M.; Wang, Y.; George, T. F.; unpublished results.

(22) Overhauser, A. W. In *Highlights in Condensed Matter Theory; International School of Physics "Enrico Fermi"*, Course 89, Bassani, F.; Fumi, F.; Tosi, M. P.; Eds., North Holland: Amsterdam, 1985; p 194. Overhauser, A. W. *Adv. Phys.* **1978**, *27*, 343.

(23) Giebultowicz, T. M.; Overhauser, A. W.; Werner, S. A. *Phys. Rev. Lett.* **1986**, *56*, 1485.

of associating $|M_S|$ with S in defining μ in eq 3 and in Figure 6]. The dependence of the UHF total energies on μ is in good agreement with a one-dimensional nearest-neighbor Ising model (IM)⁵ which leads to a linear dependence of the total energy on μ with a slope of nJ where J is the effective nearest-neighbor exchange energy. The slope of the line through the low-spin and high-spin UHF energies leads to the value $J^{\text{IM}} = -0.1514$ eV.

Both the UHF and GVB many-electron wave functions for Li_{10} are based on ten valence orbitals; however, the GVB wave function is an eigenfunction of the \hat{S}^2 operator (4) while the UHF wave function is not. The GVB calculations presented here include all possible covalent and ionic configurations and thus are the most complete for each magnetization, corresponding to the best possible wave function for Li_{10} involving ten orbitals. For all spin states, these ten GVB orbitals can be taken as D_{10h} symmetry-restricted orbitals, unlike the situation for HF or UHF. These ten GVB orbitals can be transformed to give ten Wannier orbitals; indeed the GVB low-spin Wannier orbital (Figure 7b) is virtually indistinguishable from the high-spin Wannier orbital (Figure 7a). Hence, all of the spin states calculated with the GVB wave function are consistent with the D_{10h} symmetry, leading to many-electron states with symmetries $^{11}\text{B}_{2u}$, $^9\text{A}_{1g}$, $^7\text{B}_{2u}$, $^5\text{A}_{1g}$, $^5\text{B}_{2u}$, and $^1\text{A}_{1g}$. As a result, the GVB wave functions do not contain charge density or spin density waves for any of these states of Li_{10} . The GVB results lead to a monotonic increase in the energy with increasing magnetization, with zero slope at $\mu = 0$, suggesting that the singlet-triplet splitting approaches zero as n approaches infinity.²⁴ We find that for Li_{10} the GVB spin spectrum is accurately described in terms of a nearest-neighbor Heisenberg model (HM),^{5,24} where J is chosen to match the energy difference between the $\mu = 0$ and $\mu = 1$ states, leading to a root mean square error of 0.012 eV for the four remaining spin states. For Li_{10} , this leads to $J^{\text{HM}} = -0.1415$ eV (in reasonable agreement with the Ising value $J^{\text{IM}} = -0.1514$ eV). This excellent agreement of the GVB calculations with the Heisenberg model is shown in Figure 6.

The HF wave function (C_s orbitals) contains charge density waves for the low-spin state of the Li_{10} ring cluster. The low-spin Li_{10} UHF wave function is characterized by spin density waves although it is completely free of charge density waves. The low-spin Li_{10} GVB wave function is completely free of both charge density and spin density waves.

The Li_{10} ring is stable with respect to dissociation into Li_2 molecules



by 0.243 eV/atom for the GVB wave function, 22% of the difference in stability between bulk Li and Li_2 [eq 1 and 2]. The low-spin HF wave function contains so much unfavorable ionic character that it predicts the Li_{10} ring to be *unstable* with respect to dissociation into dimers (7) by 0.054 eV/atom. The UHF results overestimate the stability of Li_{10} with respect to Li_2 dimers, giving 0.312 eV/atom. This is because the UHF wave function leads to much larger spin contamination errors for Li_2 than for Li_{10} , a result that is expected since the high-spin state is bound for Li_{10} but highly repulsive for Li_2 . The stability of Li_{10} with respect to atoms is 0.47 eV greater for GVB than for UHF (see Figure 6).

In summary, with no restrictions on symmetry (denoted as C_s in Figure 6), HF, UHF, and GVB all lead to monotonic variations in energy vs. spin. UHF agrees with GVB in favoring low spin, while HF favors high spin. Thus, the HF description of the magnon spectrum is in serious error, e.g., HF leads to a ferromagnetic (high-spin) ground state and charge density waves for all other spin states. This must not be taken lightly, since the HF, jellium,²⁰ and Hückel²¹ models are all based on molecular orbital theory.

The UHF wave function gives the correct antiferromagnetic ground state but with spin density waves for the low and intermediate spin states. The UHF spectrum of spin states is well described in terms of an Ising Hamiltonian, but leads to results

(24) Orbach, R. *Phys. Rev.* **1958**, *115*, 1181.

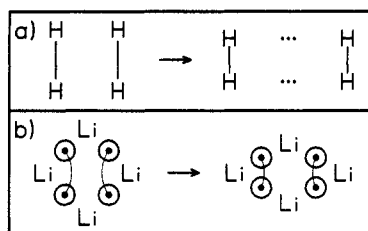


Figure 8. Geometric distortions for (a) H_4 and (b) Li_4 . The bonds for H_4 are indicated by vertical lines (the electrons are atomic centered). For Li_4 circles with dots represent the singly occupied bond-centered orbitals, while lines connecting the dots show the dominant spin pairing.

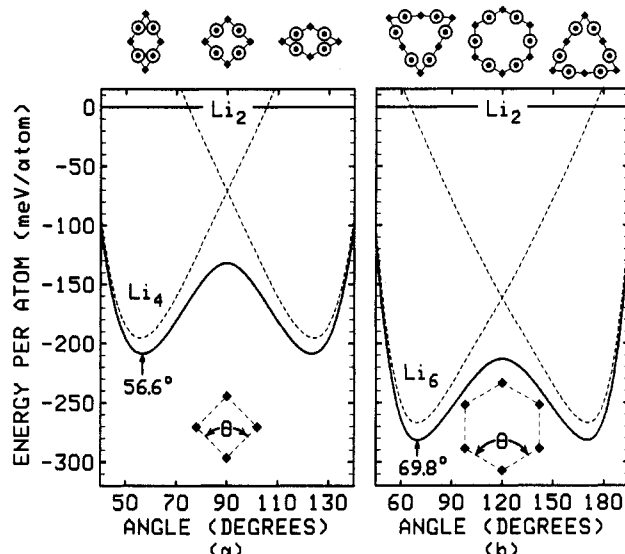


Figure 9. Potential energy curves for geometric distortions of the (a) Li_4 and (b) Li_6 clusters as a function of the bond angle, θ . In each case, the perimeters have been optimized for each value of θ . Dashed curves represent the separate resonance structures, while solid lines show the energy including all possible resonance structures. The energy per atom is given relative to Li_2 (at equilibrium). Diagrams above the plots show the cluster geometries at various angles (θ) where squares mark the atomic positions and circles mark the positions of the orbitals.

that are in disagreement with the more exact (GVB-Heisenberg) description [e.g., nonzero singlet-triplet gap for $Li_{(1D)}$].

The GVB wave functions for the various magnetizations retain full spatial and spin symmetries within a localized orbital description. Because the optimum GVB singly occupied orbitals have small overlaps, the magnon spectrum of Li_{10} (and also that of $Li_{(1D)}$) is described with excellent accuracy in terms of a simple Heisenberg Hamiltonian, where the coupling terms (J_{ij}) are extracted from the ab initio calculations.

Taken together, the GVB, UHF, and HF results in Figure 6 all indicate that it is *absolutely essential* for $Li_{(1D)}$ that each orbital is occupied with only one electron. Thus, in $Li_{(1D)}$, the bonding is dominated by the singly occupied orbitals with perturbations due to spin-pairing effects.

C. Tiny Clusters ($n \lesssim 8$). The GVB model for the 1D lithium rings and chains leads to correct predictions of the distortions that occur when the ring (or chain) structures are allowed to relax. The working principles in making these predictions for the optimum geometric distortions are (1) start with the symmetric ring geometry for neutral clusters and with the linear chain geometry for the cation or anion clusters, (2) pair up adjacent orbitals so as to maximize the number of bond pairs, (3) distort the geometry so as to increase overlaps in bond pairs by decreasing the distance between adjacent spin-paired orbitals, and (4) decrease the nonbonded repulsions (arising from orthogonalization due to the Pauli principle) by increasing the distance between adjacent orbitals that are *not* spin paired.

To illustrate how the bonding in Li_n affects geometrical structure we compare H_4 with Li_4 . In square H_4 , the optimum orbitals are

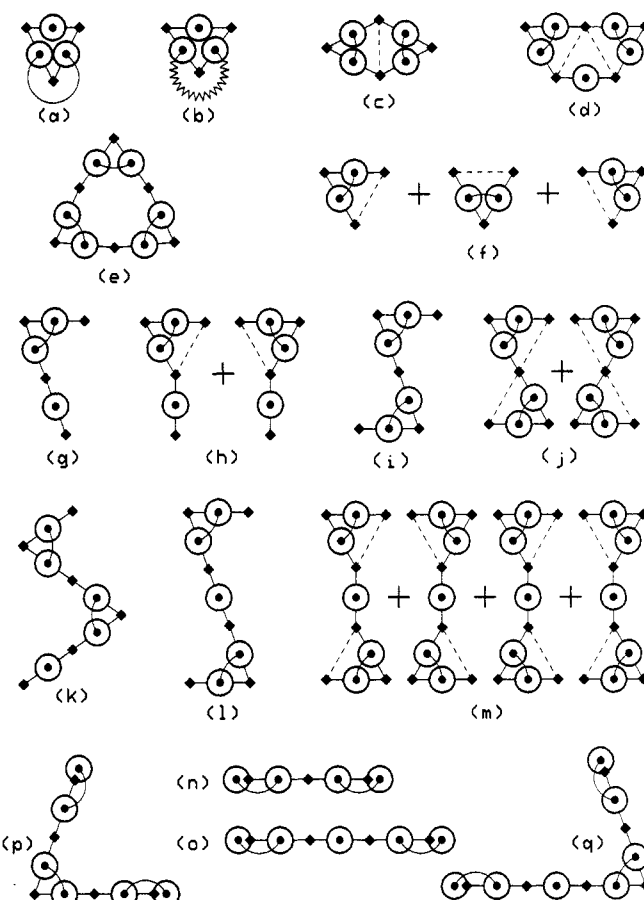


Figure 10. Low-energy isomers predicted by the 1D GVB model for (a) Li_3 saddlepoint; C_{2v} , 2A_1 , (b) Li_3 minimum; C_{2v} , 2B_2 , (c) Li_4 ; D_{2h} , 1A_g , (d) Li_5 ; C_{2v} , 2A_1 , (e) Li_6 ; D_{3h} , $^1A'_1$, (f) Li_3^+ (with resonance); D_{3h} , $^1A'_1$, (g) Li_4^+ ; C_s , $^2A'$, (h) Li_4^+ (with resonance); C_{2v} , 2A_1 , (i) Li_5^+ ; C_{2h} , 1A_g , (j) Li_5^+ (with resonance); D_{2h} , 1A_g , (k) Li_6^+ ; C_s , $^2A'$, (l) Li_6^+ ; C_{2h} , 2A_g , (m) Li_6^+ (with resonance); D_{2h} , 2A_g , (n) Li_7^- ; $D_{\infty h}$, $^1\Sigma_g^+$, (o) Li_4^- ; $D_{\infty h}$, $^2\Sigma_g^+$, (p) Li_5^- ; C_{2v} , 1A_1 , and (q) Li_6^- ; C_s , $^2A'$. Squares denote the atomic positions, circles with dots represent the singly occupied valence orbitals, and lines connecting the dots show the dominant spin pairing. In all cases the orbitals are centered on bond midpoints, and for the negative ions additional surface orbitals are present (see Figures 4 and 5). The acute bond angles range from 55° to 70° .

atom-centered. Thus the above principle leads to a rectangular distortion (see Figure 8a). Indeed, in this case the stable configuration has two separate H_2 molecules (no chemical bonding between the two H_2 fragments). On the other hand, for square Li_4 , the optimum valence orbitals are *bond-centered* so that the above principles suggest a rhombic distortion (see Figures 8b and 9a). Because of the dominance of one-electron bonding, the Li_4 cluster is stable with respect to two Li_2 molecules for both the square and rhombic geometries. Indeed, as a result of the one-electron bonds along the four edges, the optimum edge lengths (R_e) for square Li_4 ($\theta = 90^\circ$, $R_e = 3.026 \text{ \AA}$) and rhombic Li_4 ($\theta_{opt} = 56.6^\circ$, $R_e = 3.083 \text{ \AA}$) are quite similar. For both H_4 and Li_4 , the distortions away from the symmetrical geometry lower the energy of one resonance structure but raise the energy of the other resonance structure, reducing the resonance energy drastically. However, the gain in bonding for the favored structure more than compensates for the loss in resonance, and square Li_4 ($\theta = 90^\circ$) distorts to a rhombus ($\theta_{opt} = 56.6^\circ$), as indicated in Figure 9a.²⁵⁻²⁸

(25) Similar optimum geometries have been reported on Li_4 , Na_4 , and Na_6 using ab initio configuration interaction (CI) or local density functional (LDF) methods. Thus bond angles of $\theta_{opt} = 52.8^\circ$ (CI, Li_4 , ref 27), $\theta_{opt} = 53.1^\circ$ (CI, Li_4 , ref 26), $\theta_{opt} = 53.8^\circ$ (CI, Na_4 , ref 26), $\theta_{opt} = 53^\circ$ (LDF, Na_4 , ref 28), and $\theta_{opt} = 61^\circ$ (LDF, Na_6 , ref 28) were calculated.

(26) Beckmann, H.-O.; Koutecký, J.; Bonačić-Koutecký, V. *J. Chem. Phys.* 1980, 73, 5182 and ref 39.

(27) Rao, B. K.; Jena, P. *Phys. Rev. B* 1985, 32, 2058.

(28) Martins, J. L.; Buttet, J.; Car, R. *Phys. Rev. B* 1985, 31, 1804.

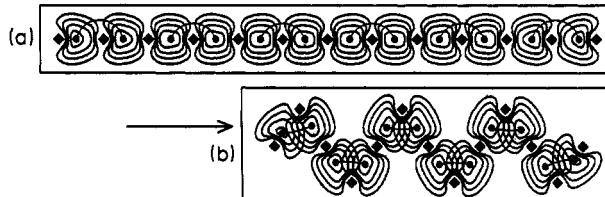


Figure 11. The GVB description of the geometric distortion of the (a) Li_{13}^+ linear chain cluster ($R = 3.12 \text{ \AA}$) into the (b) Li_{13}^+ zig-zag chain cluster ($R = 3.12 \text{ \AA}$, $\theta = 70^\circ$). In each case all 12 orbitals are shown. Contour spacings are at 0.015 au of orbital amplitude starting at 0.045 au. The atomic positions are marked by squares. Circles with dots represent the singly occupied bond-centered orbitals. Thin lines connecting the dots show the dominant spin pairing. Overlaps of adjacent spin-paired orbitals increase from ≈ 0.33 to ≈ 0.60 upon bending (a \rightarrow b).

These same bonding principles govern the structures of other tiny naked clusters as well, and predictions of the low energy planar isomers for neutral, cation, and anion clusters of three to six atoms predicted by these principles are shown in Figure 10.

Starting with hexagonal Li_6 ($\theta = 120^\circ$, $R_e = 3.079 \text{ \AA}$), these bonding principles predict a distortion to a trigonal hexagon²⁹ ($\theta_{\text{opt}} = 69.8^\circ$, $R_e = 3.064 \text{ \AA}$, Figure 10e).²⁵ Potential energy curves for this distortion are shown in Figure 9b as a function of θ [where the edge length (R) is optimized for each value of θ ³⁰]. Indeed, the optimum orbitals for planar Li_6 are centered at the surface bond midpoints.⁷ Topologically, the electronic structures of the Li_4 and Li_6 rings are equivalent to the π -electronic structures of cyclobutadiene (C_4H_4) and benzene (C_6H_6), respectively, except that the valence electrons of the lithium rings are localized on the bond midpoints while the π electrons of the CH rings are atom-centered. This suggests that both cyclobutadiene and benzene would also distort in the absence of the strong σ bonds.

For infinite 1D Li [$\text{Li}_{(1D)}$], allowing a distortion into two dimensions results in an infinite zig-zag chain (alternating 70° and 180° bond angles) as shown in Figure 11 for Li_{13}^+ . This distortion is due to the same spin-pairing and overlap effects that govern H_4 , Li_4 , and Li_6 .

The optimum structure for planar Li_5 is predicted and explained in a similar fashion. Starting with the Li_5 ring ($\theta = 108^\circ$), the GVB bonding principles suggest that the bond angle at each vertex atom shared by two adjacent orbitals of a bond pair decreases to 55 – 70° (increasing the bond pair overlaps), as shown in Figure 10d. Indeed ab initio configuration interaction (CI) calculations on Li_5 ²⁷ lead to a distorted ring geometry (two small angles of 61.2° and three large angles 120.5° , 120.5° , and 176.5°) that is consistent with this GVB description. In addition, local density functional (LDF) calculations²⁸ on Na_5 give a similar geometry (bond angles of 58.4° , 58.4° , 119.4° , 119.4° , and 184.5°). This suggests that the bonding of both Li_5 and Na_5 is dominated by electrons localized in bond midpoints.

Next we illustrate these principles for Li_3^+ and Li_3^- . Starting with linear Li_3^- , our model predicts that bending the bond angle would be unfavorable since it increases the overlap of adjacent orbitals that are not spin paired (Figure 10n). Thus, Li_3^- is linear. This is in agreement with ab initio calculations³¹ for Li_3^- . Starting with linear Li_3^+ and bending the cluster increases the bond pair overlap and hence increases the bonding. At 60° , there are three equivalent bond midpoints, and, hence, three equivalent resonance structures (Figure 10f). Consequently, the equilateral triangle is the equilibrium structure.

To analyze neutral Li_3 , we start with the equilateral triangle ($\theta = 60^\circ$). Neutral Li_3 is a special case, unlike those considered

(29) Our results for Li_4 are consistent with a pseudo-Jahn-Teller description (ref 26). However, the pseudo-Jahn-Teller description does not predict the analogous distortion for the Li_6 ring.

(30) Previous values of $\theta_{\text{opt}} = 57.3^\circ$ and $\theta_{\text{opt}} = 69.3^\circ$ for Li_4 and Li_6 , respectively, reported in ref 7 were calculated by assuming a fixed perimeter as a function of θ .

(31) Eades, E. A.; Hendewerk, M. L.; Frey, R.; Dixon, D. A.; Gole, J. L. *J. Chem. Phys.* **1982**, *76*, 3075.

TABLE I: Summary of Results Calculated for M_3

wave function	obtuse state		acute state		
	bond angle, deg	perimeter, Å	bond angle, deg	perimeter, Å	ΔE^a , meV
Li_3					
Hartree-Fock	75.4	9.361	50.5	9.065	-31.8
GVB	68.1	8.951	53.8	8.935	11.5
valence CI	71.5	9.090	52.2	9.038	8.3
valence CI ^b	71.1	8.956	53.8	8.940	6.9
Na_3 , valence CI ^c	73.4	10.57	51.5	10.63	25.9
Cu_3 , CI ^d	68.5	7.40	54.9	7.35	7.3
Ag_3 , CI ^d	69.2	8.49	55.2	8.44	13.4

^aCalculated difference in the total energy between the obtuse and acute states [the obtuse state is lower except for the uncorrelated (Hartree-Fock) wave function]. ^bReference 32. ^cReference 35. ^dReference 37.

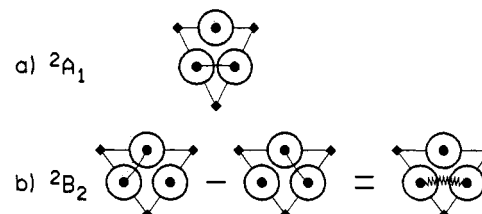


Figure 12. The GVB description of the two low-lying electronic states of Li_3 . (a) The ${}^2\text{A}_1$ saddlepoint geometry ($\theta = 52.2^\circ$) which is described by a single valence-bond resonance structure. (b) The ${}^2\text{B}_2$ equilibrium geometry ($\theta = 71.5^\circ$) which is described equally well by either the resonance of two valence-bond structures or a single structure where two electrons are high-spin coupled and the third electron is coupled to the other two electrons to form an overall spin-doublet state.

above, because of this very small bond angle and also because the equilateral triangle is the only regular polygon which cannot be distorted without changing the lengths of its sides. Thus, any variation of the bond angle to optimize the *two-electron* bonding according to the aforementioned principles is at expense of stretching or compressing *one-electron* bonds. Nevertheless, we find that the full GVB wave functions for low-lying geometries of Li_3 do indeed contain orbitals localized in bond midpoints and thus, the stationary point geometries of Li_3 can be described in terms of principles based upon orbitals localized in bond midpoints.

Results for Li_3 are presented in Table I and Figure 12. Pairing two orbitals to form a bond pair favors distortion (at the shared atom) to a smaller angle ($\theta_{\text{opt}} = 52.2^\circ$) in order to increase the overlap of the bond pair of electrons and to decrease the interaction of the radical orbital with the bond pair ($\theta_{\text{opt}} = 63.9^\circ$). This leads to the ${}^2\text{A}_1$ state (acute bond angle) as shown in Figure 12a. A second low-lying state results from a resonance superposition of two primary resonance structures (see Figure 12b). This resonance superposition of two primary resonance structures is very similar to the spin coupling in the π -electron system of the allyl radical.³³ This resonance description is equivalent to an independent particle description composed of the triplet pairing of two electrons (indicated by jagged lines) and coupling with the remaining electron to obtain a spin doublet state (the "GF"^{18,33} spin coupling). In this case, the bond angle at the atom shared by the triplet-coupled electrons must increase, leading to an "obtuse" isosceles triangular structure (${}^2\text{B}_2$) with apex angle of 71.5° .

Both the acute and obtuse structures are low-lying for Li_3 . The global minimum of Li_3 is the GF spin-coupled "obtuse" triangle geometry (Figure 12b), while the valence-bond spin-coupled "acute" triangle geometry (Figure 12a) is 8.3 meV higher, representing the barrier to pseudorotation. The Hartree-Fock results (which neglect electron correlation effects) also indicate that both the acute and obtuse states are low-lying; however, Hartree-Fock

(32) Bagus, P. S.; del Conde, G.; Davies, D. W. *J. Chem. Soc., Faraday Discuss.* **1977**, *62*, 321.

(33) Levin, G.; Goddard III, W. A. *J. Am. Chem. Soc.* **1975**, *97*, 1649. *Theor. Chim. Acta* **1974**, *37*, 253.

yields the wrong ground state. The results of GVB calculations on Li_3 are in very good quantitative agreement with full valence CI results within the same valence double- ζ basis set and with other full valence CI calculations³² with regard to the stationary point geometries and barrier to pseudorotation. Similar results have been found for other alkali trimers^{35,36} as well as for Cu_3 ^{37,38} and Ag_3 ,³⁷ indicating that the bonding mechanism is at least qualitatively similar for all of these systems. Results for Na_3 ,³⁵ Cu_3 ,³⁷ and Ag_3 ,³⁷ are included in Table I for comparison. The importance of the one-electron bonding in these systems is illustrated by the similarity of the perimeters (obtained by adding the three bond lengths) for the acute and obtuse states.

Low-lying isomers for the larger charged clusters ($\text{Li}_{4,5,6}^{+,+}$) are predicted in a similar fashion by starting with the principle resonance structures of the linear chain clusters and varying the angles as described above. The predicted low-energy isomers for all of these clusters are also shown in Figure 10. The electronic structures for these isomers are indicated with circles with dots representing the singly occupied orbitals and lines connecting the dots indicating the dominant spin pairing. The isomers (l) and (m) of Li_6^{+} are expected to have very little barrier to rotation about the central bond midpoint into a three-dimensional structure where the two planar Li_3 subunits are staggered. Similarly, the isomers for Li_5^{+} are expected to exhibit free rotation about the central atom.

Because of the multitude of "reasonable" structures for metallic clusters, it is very important to have a correct set of guidelines such as those given in this section if one is to correctly determine the low-energy isomers. Previous theoretical approaches to determining the low-energy isomers have been to guess structures, and then calculate their energies. Thus, in the first high-quality (electron correlation inclusive) ab initio studies on Li clusters,³⁹ the correct structure of Li_4 was obtained and a D_{4h} oblate octahedron structure for Li_6 was proposed based on the Li_4 structure. In a subsequent multiple-reference singles and doubles CI ab initio investigation,⁴⁰ it was determined for Li_6 that the lowest energy structure was a C_{5v} pyramid, with the planar structure (similar to that of Figure 10e but $\theta = 60^\circ$ was assumed) and the D_{4h} structures higher in total energy by 0.045 and 0.194 eV, respectively. In an improved multiple-reference singles and doubles CI ab initio investigation using modified virtual orbitals,⁴¹ it was determined for Li_6 that the 60° planar structure is indeed the lowest energy structure, with the C_{5v} and D_{4h} structures higher in total energy by 0.039 and 0.240 eV, respectively. These studies were performed with complete geometry optimizations with the exception that planar isomer was optimized with the $\theta = 60^\circ$ angle restriction. Thus, relaxing geometric restrictions for all isomers will result in an increase of θ and thus an increase of the stability of the planar isomer over the other isomers for Li_6 .

More recently, gradient approaches have been utilized to determine the forces on guess structures to obtain stationary isomers.^{27,28} However, these approaches have been limited to eight or less atoms and may be somewhat sensitive to the initial starting structures, especially if there are energy barriers separating the various low-energy isomers.

The general picture that is consistent with a number of theoretical studies^{27,28,41} and our own preliminary calculations³⁴ is that these "1D zig-zag" clusters are competitive up to $n \approx 8$. The

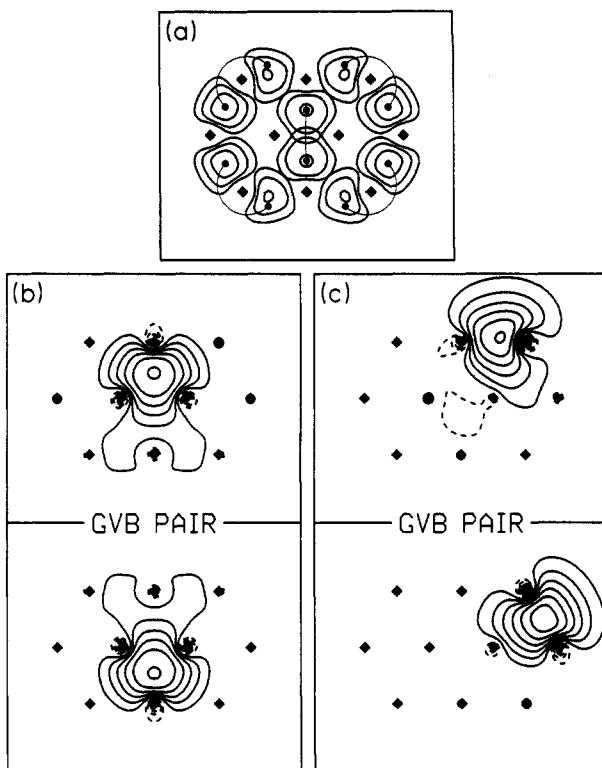


Figure 13. (a) All ten singly occupied GVB orbitals for the principal resonance structure of planar close-packed Li_{10} ($R = 3.1 \text{ \AA}$; contour increments starting at 0.060 au). Squares mark the atoms, and dots joined by thin lines represent the paired electrons. (b) Bulk bond pair, 0.71 overlap. All contours are included. (c) Surface bond pair, 0.50 overlap. All contours are included.

zig-zag Li_8 cluster puckers out of the plane in a fashion similar to cyclohexane. As the clusters increase in size, there is a tendency toward forming more compact structures (e.g., planar close-packed structures for the very small clusters), due to the resonance and/or delocalization stability obtained by increasing the number and/or quality of sites to place the electrons.

D. Two-Dimensional Clusters. The optimum planar structures for Li_4 , Li_5 , and Li_6 resemble planar close-packed clusters. Examining larger 2D close-packed arrays of Li atoms, we find the general result that *interior regions* have singly occupied orbitals localized at the *centers of equilateral triangles* while *surface (edge) regions* have singly occupied orbitals localized at *bond midpoints*. This is illustrated for planar Li_{10} in Figure 13. Extrapolating to the infinite 2D (close-packed) system [$\text{Li}_{(2D)}$] leads to the description in Figure 14a where alternate pairs of triangular hollows have bond pairs and triangular hollows adjacent to the bond pairs are empty.

This GVB description for $\text{Li}_{(2D)}$ could lead to charge density waves (CDW). However, there are an infinite number of ordered and disordered resonance structures (such as those shown in Figure 14b-c) that may enter into the many-electron wave function. Charge density waves have been proposed to account for certain experimental electronic anomalies for bulk (3D) alkali metals²² and have recently been observed by neutron diffraction for bcc potassium.²³ It is interesting to speculate whether the present GVB model involving the spin-pairing localized interstitial orbitals would lead to CDW in bcc, hcp, or fcc bulk metals.

This GVB description for $\text{Li}_{(2D)}$ may lead to metallic character. Half of the triangular hollows are empty, providing low-lying charge-transfer states required for conduction. The existence of essentially an infinite number of disordered resonance structures such as that shown in Figure 14c suggests a high density of low-lying many-electron states.

E. Three-Dimensional Clusters. We next discuss the GVB wave functions for Li_{13}^{+} clusters having one central (bulk) atom and twelve surface atoms. The three high-symmetry structures examined, listed in order of increasing energy, are (1) I_h , the

(34) McAdon, M. H.; Goddard III, W. A., unpublished results.

(35) Martin, R. L.; Davidson, E. R. *Mol. Phys.* **1978**, *35*, 1713.

(36) Thompson, G. A.; Lindsay, D. M. *J. Chem. Phys.* **1981**, *74*, 959.

(37) Walch, S. P.; Bauschlicher, C. W.; Langhoff, S. R. *J. Chem. Phys.* **1986**, *85*, 5900.

(38) Moskovits, M. *Chem. Phys. Lett.* **1985**, *118*, 111. Also see Lindsay, D. M.; Thompson, G. A.; Wang, Y. Presented at the 191st National Meeting of the American Chemical Society, New York, NY, April 13-18, 1986, appearing elsewhere in this issue.

(39) Beckmann, H.-O.; Koutecký, J.; Botschwina, P.; Meyer, W. *Chem. Phys. Lett.* **1979**, *67*, 119.

(40) Plavšic, D.; Koutecký, J.; Pacchioni, G.; Bonačić-Koutecký, V. J. *Phys. Chem.* **1983**, *87*, 1096.

(41) Fantucci, P.; Bonačić-Koutecký, V.; Koutecký, J. *J. Comput. Chem.* **1985**, *6*, 462.

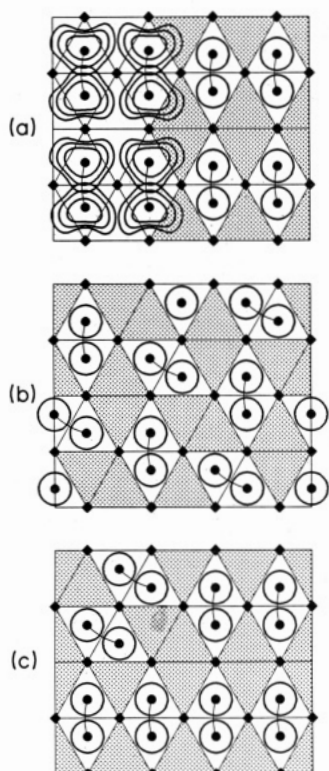


Figure 14. (a) The GVB description of $\text{Li}_{(2D)}$. The upper left corner shows contours $\geq 0.060 \text{ au}$ for eight GVB orbitals optimized without restriction for the planar Li_{12}^{4+} cluster. The edge atoms of a planar unit cell count half, since each contributes half an electron to the cell and half an electron to the adjacent cell. Hence, the model Li_{12}^{4+} cluster is composed of four unit cells (two atoms per cell) with a total of eight valence electrons. The orbitals for the planar Li_{12}^{4+} cluster were obtained for 12 "real" atoms (four GVB pairs, 0.52 overlap each pair). The description of $\text{Li}_{(2D)}$ is obtained by translation of the planar Li_{12}^{4+} cluster where connected circles represent the singly occupied orbitals and shaded triangles represent empty hollows. (b) An alternative ordered resonance structure for $\text{Li}_{(2D)}$. (c) A disordered resonance structure for $\text{Li}_{(2D)}$.

TABLE II: Relative Energies of Li_{13}^+ Clusters^a

cluster	structure	relative energy	
		total, eV	per atom, meV/atom
OPTET(I)	$\gamma-(4,4,5), C_{2v}$	0.000	0.0
OPTET(II)	$\gamma-(4,4,4,1), C_s$	0.057	4.4
OPTET(III)	$I_h(1,11,2), C_{2v}$	0.197	15.1
planar	C_{2v}	0.400	30.8
icosahedron	$I_h(1,12), I_h$	0.581	44.7
fcc	$(1,12), O_h$	0.837	64.4
zig-zag chain	C_{2h}	0.947	72.9
hcp	$(1,12), D_{3h}$	1.144	88.0
linear chain	$D_{\infty h}$	1.678	129.1

^aThe structures are shown in Figures 11, 15–17, 19, and 20. Results are calculated at the GVB-CI level with basis set D. See the Appendix and Table VI for further details.

icosahedron; (2) fcc, the truncated octahedron corresponding to the nearest neighbors of a face-centered cubic lattice; and (3) hcp, the hexagonal array corresponding to the nearest neighbors of a hexagonal close-packed lattice. We will concentrate our studies here on the positive ion, Li_{13}^+ , since all the electrons can be spin paired, providing a useful model for the bonding in large clusters. Also, positively charged metal clusters have been examined experimentally and hence techniques to test the predictions may soon become practical. The results are given in Table II (see the Appendix for details).

The I_h cluster (Figure 15) ground state involves electrons localized at the centers of twelve of the twenty triangular faces. Each electron is spin-paired to an electron in an adjacent (edge-shared) surface triangle to form a rhombus (0.63 overlap)

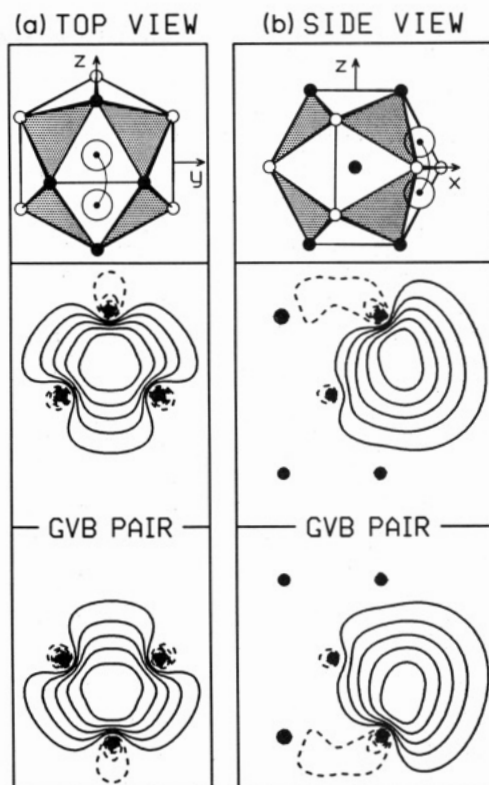


Figure 15. GVB orbitals for one of the six equivalent bond pairs of icosahedral Li_{13}^+ (six pairs occur along the $\pm x$, $\pm y$, and $\pm z$ directions; the $+x$ pair is shown). (a) The top view where the orbital contours in the surface planes are shown. (b) A side view where the orbital contours in a symmetry plane bisecting the cluster are shown. In each case, the atoms in the plotting plane are marked by filled circles while atoms above and below that plane are marked by open circles. Connected dots represent the spin-paired electrons. Shaded triangular faces do not contain orbitals. Overlaps of spin-paired orbitals are 0.63.

just as for the bulk electrons of $\text{Li}_{(2D)}$ (Figures 13 and 14). The four triangular faces adjacent to a spin-paired rhombus are empty (to avoid repulsive interactions between unpaired electrons), as indicated in Figure 15. Each of the twelve $I_h \text{Li}_{13}^+$ valence orbitals is equivalent. Figure 15 shows the GVB electron pair on the $+x$ axis. The many-electron wave function is composed of six equivalent such GVB pairs (one GVB pair along each of the $\pm x$, $\pm y$, and $\pm z$ axes).

The fcc cluster (Figure 16) has only eight tetrahedra (rather than the twenty of I_h). These eight tetrahedra are all geometrically equivalent and have three interior edges and three surface edges. Each interior tetrahedral edge is shared by two tetrahedra; thus, each tetrahedron shares an edge with three other tetrahedra. We find that all twelve singly occupied valence orbitals localize among the eight tetrahedra of the fcc cluster, leading to a total energy for the fcc cluster 0.26 eV higher than that for I_h (20 meV/atom). Four tetrahedra each have two orbitals (centered on opposite faces, spin-paired with 0.75 overlap), accounting for eight of the twelve valence electrons. These doubly occupied tetrahedra are staggered so that no doubly occupied tetrahedron shares an edge with any other doubly occupied tetrahedron. The other four tetrahedra each have only one orbital (centered on an exterior face), accounting for the four remaining valence electrons. The four electrons in the singly occupied tetrahedra are well separated from one another, leading to a ground-state singlet having two weakly coupled bond pairs (-0.28 overlap for each pair). The optimum singly occupied orbitals for fcc Li_{13}^+ are shown in Figure 16 for each type of bond pair. Focusing on a tetrahedron containing two electrons, one finds that the three adjacent edge-sharing tetrahedra each contain only one electron (in order to avoid the repulsive interactions endemic to two sets of paired electrons).

The hcp cluster (Figure 17) also has eight tetrahedra; however, six of the tetrahedra for hcp occur in pairs sharing one face, while

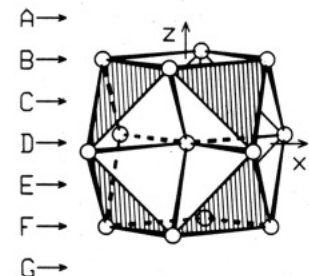
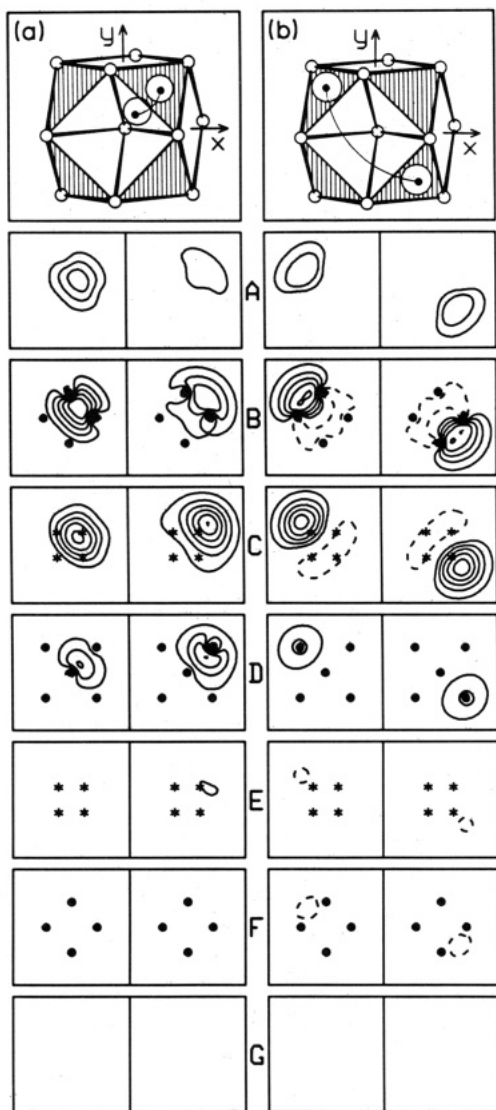


Figure 16. GVB orbitals for the two types of bond pairs in the fcc Li_{13}^+ cluster. (a) The two spin-paired orbitals located in the doubly occupied 111 tetrahedron and (b) the orbital localized in the singly occupied 111 tetrahedron (and spin-paired with the orbital of the 111 tetrahedron). Here cross sectional amplitudes of each of the orbitals are given at different evenly spaced (001) planes. Planes B, D, and F pass through atoms, marked by filled circles. Planes C and E pass through the centers of tetrahedral hollows, marked by asterisks. Planes A and G pass through virtual tetrahedral centers.

the other two are isolated, sharing edges with the above paired tetrahedra. The result is a total energy 0.56 eV higher than I_b (43 meV/atom). The three face-shared tetrahedral pairs each have one set of spin-paired orbitals, with one electron localized in the tetrahedron above the shared face and one electron localized below the shared face. This accounts for six valence electrons (three GVB pairs with overlaps of 0.58, 0.58, and 0.62). The two remaining tetrahedra each contain one spin-paired set of orbitals (four electrons, two GVB pairs, 0.78 overlap). The remaining two electrons cannot go into tetrahedra without a severe energetic

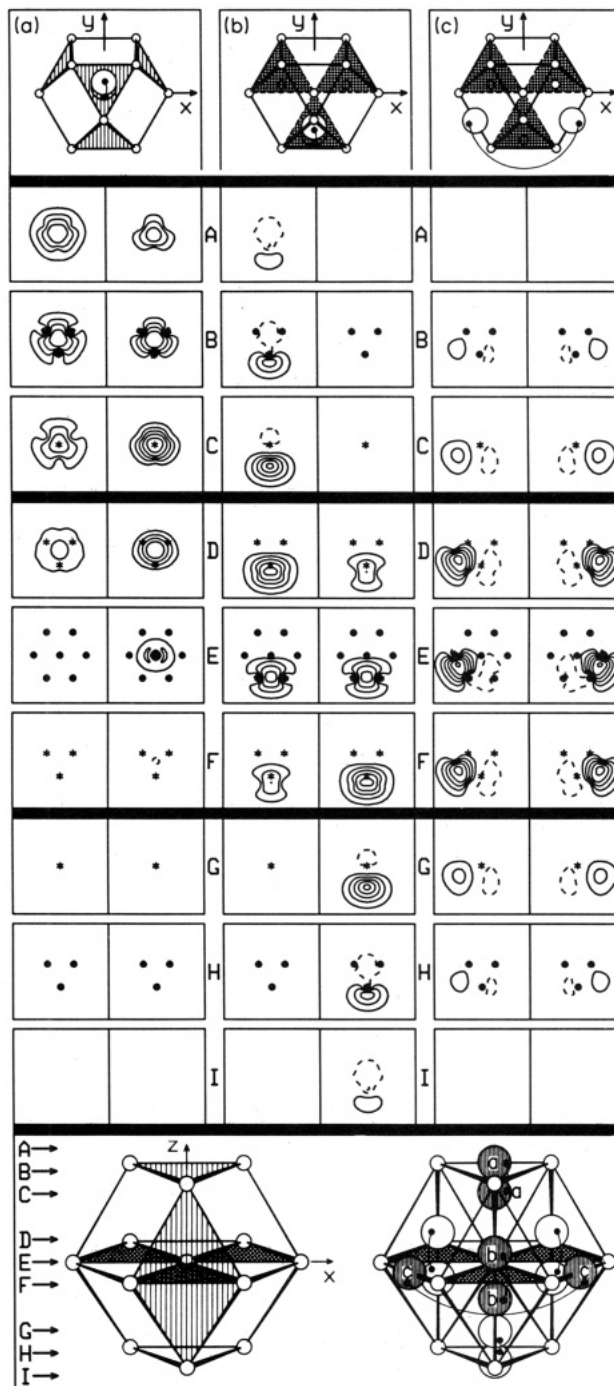


Figure 17. GVB orbitals for the three types of bond pairs in the hcp Li_{13}^+ cluster. (a) A spin-paired set of orbitals located in a doubly occupied tetrahedron. (b) A spin-paired set of orbitals distributed over a face-shared pair of tetrahedra. (c) A spin-paired set of orbitals distributed over two bond midpoints. Here, cross-sectional amplitudes of the orbitals are given at nine (0001) planes intersecting the z axis at $z = 1.25, 1.0, 0.75, 0.25, 0.0, -0.25, -0.75, -1.0$, and -1.25 (in units of $c/2$, where c is the length of the hcp unit cell in the z direction). Planes B, E, and H intersect atomic positions, marked by filled circles. Planes C, D, F, and G pass through the centers of tetrahedra, marked by asterisks. Planes A and I pass through virtual tetrahedral centers in the vacuum, e.g., tetrahedra that would be present if the cluster were allowed to grow in the $\pm z$ directions.

penalty; placing a third electron in a face-sharing pair of tetrahedra leads to very strong antibonding interactions. Consequently, the last two electrons end up along two of the three equatorial edges that do not border a tetrahedron (one GVB pair, -0.36 overlap). Summarizing, ten of the twelve valence electrons occupy tetrahedra, while the remaining two valence electrons occupy surface bond midpoints (that do not border tetrahedra). These optimum

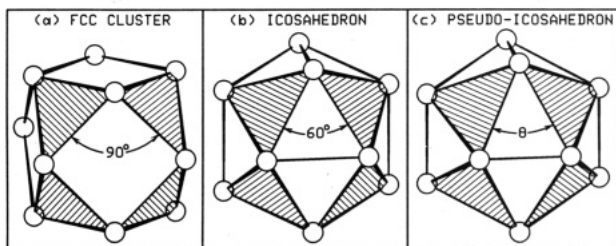


Figure 18. The Jahn-Teller-like distortion of the Li_{13}^+ icosahedron cluster leading to a pseudo-icosahedron. (a) The fcc cluster (cubo-octahedron, O_h symmetry). (b) The icosahedron (I_h symmetry), formed by compressing the square faces of the fcc cluster ($\theta = 90^\circ$) into rhombi ($\theta = 60^\circ$). (c) The pseudo-icosahedron (T_h symmetry) formed by further compressing the same faces ($\theta < 60^\circ$). The T_h point group symmetry is preserved for all θ .

singly occupied orbitals for hcp Li_{13}^+ are indicated in Figure 17 for the three types of bond pairs.

The GVB descriptions for these three highly symmetrical clusters all involve breaking the high symmetry. Thus, there will be a separate resonance structure for each symmetry operation that takes the localized bonding structure into a new equivalent (but not identical) structure. Including all of these resonance structures in the many-electron wave functions leads to degenerate states and thus the resonance energy is small and Jahn-Teller-like distortions shall occur. For example, the GVB description of I_h Li_{13}^+ leads to five equivalent resonance structures which split into a quadruply degenerate ground state 1G_g and a nondegenerate excited state 1A_g . The energy lowering of the 1G_g state relative to the energy of one resonance structure is expected to be approximately one fourth that of the energy raising of the 1A_g state relative to the same reference energy.⁹ The 1G_g state is thus subject to a Jahn-Teller-like distortion. If we assume that the optimum distortion can be determined by analyzing the dominant spin pairing of just one of the resonance structures (as is true for H_4 , Li_4 , Li_6 , and linear Li_{13}^+ , see Figures 8, 9, and 11) then the optimum structure of the icosahedral-like Li_{13}^+ isomer is expected to be a 1A_g state of T_h symmetry (T_h is a subgroup of both I_h and O_h , and D_{2h} is a subgroup of T_h). This T_h structure can be described by starting with the fcc cubo-octahedral structure, squashing the square faces to form the icosahedron, and then further squashing to form the optimum pseudo-icosahedral isomer, as shown in Figure 18. Such a distortion is expected to result in improved overlaps in the six equivalent bond pairs, since the dihedral angle between adjacent paired faces is reduced. Similar distortions are predicted for the fcc and hcp clusters; however, since all of these clusters are highly coordinated, such distortions may be rather small (unlike the cases for the Li_4 square or the Li_6 hexagon), leading to relatively small lowerings of the total energy.

From the results on the three high-symmetry Li_{13}^+ clusters, it is clear that the valence electrons prefer to localize in interstitial regions (tetrahedra). Using a set of concepts derived from these results (as embodied in the set of rules of section IV), we considered arrangements of 13 atoms that maximize the number of tetrahedra under the restriction that the number of tetrahedra shared by any given atom should be relatively small (much less than 20). This restriction stems from the observation that twelve valence electrons cannot all simultaneously bond in an effective manner to one central atom. Thus, the valence electrons for the I_h cluster are centered at surface triangular hollows whereas the exact tetrahedral centers are the preferred sites (in the absence of the large orthogonality and electron-electron repulsion effects associated with too many electrons trying to bond to the same central atom). This led to the prediction of several new Li_{13}^+ clusters (Figure 18) each with 15 tetrahedra.

GVB calculations show that each of these three clusters, denoted as OPTET (optimum tetrahedral), is lower in energy than I_h . These OPTET isomers all lead to local fivefold symmetry axes as a consequence of the efficient packing of tetrahedra. Two of the three OPTET clusters (I and II) also clearly coincide with

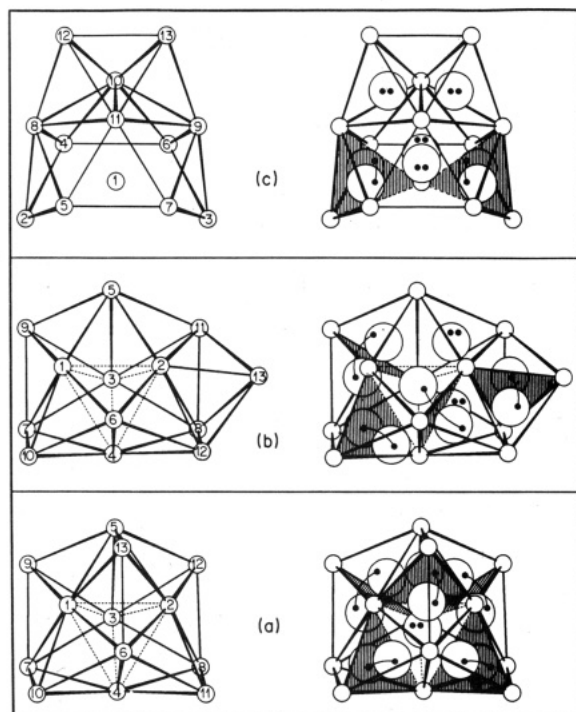


Figure 19. Three low-lying OPTET Li_{13}^+ isomers. (a) OPTET(I) which consists of a central tetrahedron (atoms 1–4, joined by dotted lines), four capping atoms (atoms 5–8), and five bridging atoms (atoms 9–13). (b) OPTET(II) which differs from OPTET(I) in the position of only one atom (atom 13). (c) OPTET(III) which consists of a central atom (atom 1) surrounded by ten atoms in the first shell (atoms 2–11 forming an incomplete icosahedral shell) and two atoms in the second shell (atoms 12 and 13). In each case, the nuclear framework is shown on the left-hand side and the electronic structure is shown schematically on the right-hand side. The positions of doubly occupied tetrahedral hollows are shown with a large circle (representing the pair of orbitals) filled by two dots (representing the electrons). The positions of singly occupied orbitals and the principle spin pairing are represented by large circles filled with one dot each, joined by thin arcs. Faces shared by singly occupied tetrahedra are shaded. OPTET clusters (I), (II), and (III) have symmetries C_{2v} , C_s , and C_{2v} , respectively. All three clusters have multiple local fivefold symmetry axes.

truncations of the γ -brass structure. The correspondence of the third structure to a truncation of γ -brass is rather subtle; OPTET(III) is more clearly based on a modification of the icosahedron. It is convenient to label these OPTET clusters in terms of their overall point group symmetries and the number of atoms in successive shells for the respective structure type. With this convention, the OPTET(I) structure is referred to as γ -(4,4,5), C_{2v} . The OPTET(II) [γ -(4,4,4,1), C_s] and OPTET(III) [I_h -(1,10,2), C_{2v}] have total energies higher than OPTET(I) by 0.05 and 0.20 eV, respectively. The high-symmetry I_h , fcc, and hcp clusters have total energies higher than OPTET(I) by 0.58, 0.84, and 1.14 eV, respectively (see Table II).

Of all Li_{13}^+ structures examined, the OPTET(I) cluster (Figure 19a) has the lowest total energy. The geometric and electronic structures of the OPTET(I) cluster are described as follows. The central tetrahedron formed by atoms 1, 2, 3, and 4 is doubly occupied (two electrons, two orbitals, 0.72 overlap). Four capping atoms (atoms 5–8 in Figure 19a) form four tetrahedra sharing faces with the central tetrahedron. Each of these four capping tetrahedra are empty (i.e., orbitals are not centered on these four capping tetrahedra; however, orbitals centered on adjacent tetrahedra have amplitudes that diminish as they approach the centers of these four tetrahedra). The five remaining atoms (labeled 9–13 in Figure 19a) form bridges to the four central atoms and to the capping atoms, leading to a total of ten new tetrahedra, each sharing one edge with the central tetrahedron and one face with the four empty tetrahedra. Each of these ten tetrahedra is singly occupied, and these ten electrons partition into five face-sharing bond pairs. We shall denote such face-sharing bond pairs

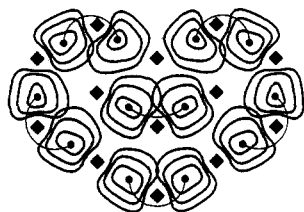


Figure 20. GVB orbitals for planar close-packed Li_{13}^+ . Only contours $\geq 0.060 \text{ au}$ are shown (0.015- au spacings). The overlap of the bulk bond pair is 0.60. The average overlap for surface bond pairs is 0.52. Squares mark the atomic positions. The dominant spin pairing is shown by the connected dots.

as $a-(b,c,d)-e$ where $a-b-c-d$ and $b-c-d-e$ indicate the two tetrahedra and (bcd) denotes the shared face. Hence, the bond pairs $5-(1,3,9)-7$, $5-(2,3,11)-8$, $6-(1,4,10)-7$, and $6-(2,4,12)-8$ each have an overlap of 0.57 and the remaining $5-(1,2,13)-6$ bond pair has an overlap of 0.66. As discussed above, this sequence starts with a tetrahedron, capping the faces and bridging the edges, leading to the characteristic cluster of the γ -brass structure. Consequently, we denote OPTET(I) as $\gamma-(4,4,5)$, C_{2v} .

The OPTET(II) cluster is just 0.057 eV higher in total energy than OPTET(I). The OPTET(II) structure differs from the OPTET(I) structure by moving one atom from the third γ -brass shell to the fourth γ -brass shell so it is denoted as $\gamma-(4,4,4,1)$, C_s . The electronic structure of the OPTET(II) ground state is diagrammed in Figure 19b. The 2-3-4-8 tetrahedron is located near the center of the cluster (on the symmetry plane) and is doubly occupied (0.72 overlap). Three tetrahedra sharing faces with the 2-3-4-8 tetrahedron are empty (1-2-3-4, 2-3-8-11, and 2-4-8-12). The 2-3-5-11 tetrahedron is also doubly occupied (0.71 overlap) and shares the 2-3 edge with the doubly occupied 2-3-4-8 tetrahedron. The remaining eight electrons occupy separate tetrahedra and are divided into four face-sharing bond pairs. These four remaining bond pairs are 11-(2,8,13)-12, 0.63 overlap; 5-(1,3,9)-7, 0.62 overlap; 6-(1,4,10)-7, 0.64 overlap; and 1-(2,4,6)-12, 0.63 overlap. With just one exception, tetrahedra sharing faces with these six bond pairs are empty. The exception to this rule is exhibited by two singly occupied tetrahedra (1-2-4-6 and 1-4-6-10). These tetrahedra share the 1-4-6 face but their electrons are not spin-paired with one another. A careful examination of these two orbitals shows that they are staggered in order to reduce the nonbonded repulsions. The 1-2-4-6 orbital is strongly polarized toward the 1-2-6 face while the 1-4-6-10 orbital is strongly polarized toward the 4-6-10 face; thus, these two orbitals have only one atom in common (atom 6).

The OPTET(III) structure (Figure 19c) is derived by plucking two adjacent atoms away from the surface of the high symmetry I_h cluster and adding them to adjacent capping positions on the opposite surface. This cluster is denoted as $I_h-(1,10,2)$, C_{2v} and leads to a total energy 0.20 eV higher than OPTET(I) but 0.38 eV lower than I_h . The electronic structure of the OPTET(III) ground state (Figure 19c) consists of four doubly occupied tetrahedra, four singly occupied tetrahedra (divided into two face-sharing pairs), and seven empty tetrahedra. Two edge-sharing tetrahedra (8-10-11-12 and 9-10-11-13) are each doubly occupied (0.67 overlap each pair). Two additional atom sharing tetrahedra (1-5-7-11 and 1-4-6-10) are also both doubly occupied (0.74 overlap each pair). All seven tetrahedra sharing faces with these doubly occupied tetrahedra are empty. The remaining four electrons are divided into two face sharing tetrahedral pairs; 4-(1,2,8)-5 and 6-(1,3,9)-7, 0.56 overlap each pair. Each of these four singly occupied tetrahedra shares one edge with a doubly occupied tetrahedron.

Summarizing, we find typical orbital overlaps are 0.74–0.78 for doubly occupied tetrahedra. Face-sharing singly occupied tetrahedral orbitals typically have overlaps in the range of 0.57 to 0.63. Overlaps outside these ranges result occasionally from atypical surroundings [e.g., adjacent tetrahedra that are empty or doubly occupied].

With such small clusters, surface effects are quite large so that planar clusters (which lead to an increased number of internal

sites) are quite competitive. Thus the planar cluster of Figure 20 has an energy 0.18-eV lower than I_h [0.40-eV higher than OPTET(I)]. Although the linear chain cluster is not a competitive structure [1.68 eV higher in total energy than OPTET(I)], the zig-zag chain cluster formed by bending the chain at alternate atomic sites (increasing bond pair overlaps as shown in Figure 11) is 0.20 eV lower in total energy than the hcp cluster [the zig-zag chain is 0.95 eV higher in total energy than OPTET(I)].

IV. Discussion

The results discussed in section III have led to a new generalized valence bond model of metallic bonding based on electrons localized in interstitial regions such as bond midpoints (1D clusters), triangular faces (2D clusters), and tetrahedral hollows (3D clusters). In section IVA we illustrate the use of these basic concepts by applying them to predictions concerning the Li_4 tetrahedron. This GVB model for metallic bonding is summarized in section IVB by a set of rules that applies to three-dimensional clusters. These rules lead to the prediction that OPTET clusters are the most stable (lowest energy) structures for naked lithium clusters from eight atoms up to about forty atoms. These OPTET clusters are discussed in section IVC. The use of these rules to rationalize properties of condensed systems (bulk solids) is illustrated in sections IVD and IVE where we examine the structures, conductivities, and solid solubility limits of bulk close-packed metals. This GVB model of metallic bonding also suggests a new type of metallic force field which should lead to improved modeling of metallic systems containing thousands of atoms (section IVF).

A. Analysis of the Li_4 Tetrahedron. To illustrate the concepts of this GVB model of metallic bonding, consider the Li_4 system. A simple model of bonding in terms of pairwise additive potentials would lead to the result that the tetrahedron is favored over the rhombus and other structures for Li_4 (it has one extra “bond”). Indeed, the results of the previous section might suggest that the four orbitals of tetrahedral Li_4 are localized on the four faces and spin-paired. The problem with this is that the distance between orbitals in different pairs would be quite small ($0.41R$), leading to large repulsive interactions. (As in the previous section, R denotes the *nearest-neighbor distance*, e.g., for tetrahedral Li_4 , R is the edge length.) Indeed, we find from GVB calculations that the optimum orbitals of the Li_4 tetrahedron are instead localized on four of the six edges and spin-paired so that orbitals in different pairs are at least $0.5R$ apart. However, starting with this description, one would expect (and we find) that the distortion to a planar (rhombic) structure is favored (leading to a distance of $0.89R$ between nonpaired orbitals). Thus, the GVB bonding principles predict (and the calculations confirm) that the stable geometry of Li_4 is the rhombus (planar).

B. The Rules. From the results on three high-symmetry clusters, it is clear that the optimum bonding involves valence electrons that prefer to localize in separate tetrahedral hollows. This suggests that the *optimum structures* of small clusters are those that *maximize the number of tetrahedra*, as is the case for I_h , with 20 tetrahedra. However, for the icosahedron, the 20 tetrahedral hollows all share the *same* central bulk atom (the eight tetrahedra for the fcc and hcp clusters also all share the central atom; see Figures 15–17). This is unfavorable for the following reasons.

(1) To describe an orbital localized in a tetrahedral interstitial requires a hybrid combination of the valence orbitals from each of the four atoms of the tetrahedron, with an equal contribution from each atom. For lithium, the low-lying orbitals are 2s and 2p and hence, each atom can contribute effectively to only four orthogonal interstitial orbitals (with the overlapping orbitals of a bond pair, one might be able to describe up to two electrons per orthogonal orbital and hence a total of eight electrons near one atom).

(2) The orthogonality induced (Pauli principle) repulsion between orbitals that are *not* spin-paired becomes large when these orbitals are close (as they must be when sharing a common vertex).

Thus, the three OPTET clusters (Figure 19) and the planar cluster (Figure 20) are all lower in energy than the I_h cluster (Figure 15).

From the results on the various clusters, we have abstracted the following rules for three-dimensional metallic structures.

(α) Orbitals (each with one electron) are localized in different tetrahedral hollows where possible.

(β) If necessary, two electrons may be placed in one tetrahedron (localizing on opposite faces or edges) but they must be spin-paired.

(γ) No more than two electrons may be distributed between a pair of *face-shared* tetrahedra, and these must be spin-paired (singlet).

(δ) No more than three electrons may be distributed between a pair of *edge-shared* tetrahedra.

(ϵ) No more than four bond pairs of electrons may share one central bulk atom, and no more than three bond pairs of electrons may share one central surface atom.

(ζ) Additional electrons must be in surface orbitals at edge or face sites that do not share edges with occupied tetrahedra.

The above principles are consistent with the calculated wave functions and total energies where the OPTET(I) cluster is lowest, with I_h , fcc, and hcp higher by 0.58, 0.84, and 1.14 eV, respectively.

C. OPTET Clusters. At this point, it is appropriate to note that infractions of the above rules for *small* clusters are unavoidable and thus are tolerated to a certain degree by such small clusters; e.g., orbitals that may prefer to be localized in tetrahedra may polarize strongly toward faces or even edges under certain circumstances in order to minimize nonbonded (orthogonality induced) repulsions. For example, although the three OPTET clusters are all composed solely of surface atoms, OPTET(I) contains two atoms each involved in four bond pairs (in violation of rule ϵ ; furthermore, these two atoms are *adjacent*). OPTETS (II) and (III) each contain one such atom. In addition, OPTETS (II) and (III) each have a single infraction against rule δ (edge-sharing), while OPTET (II) also has a single violation against rule γ (two orbitals in face-shared tetrahedra that are not spin-paired). Overall, this accounts for two infractions for OPTETS (I) and (III) and three infractions for OPTET(II). Thus, the explanation of the relatively high energy of OPTET(III) in comparison with OPTETS (I) and (II) lies in the relatively large number of doubly occupied tetrahedra [four for OPTET(III) vs. one for OPTET(I) and two for OPTET(II)].

We have shown in section IIIB that the electronic structures of very small clusters (less than eight atoms) are characterized by electrons localized in bond midpoints, leading to very small bond angles (57–70°). Our various calculations indicate that the OPTET or γ -brass structures should be the most stable for clusters as small as Li_8 [γ -(4,4), T_d] up to clusters as large as 40 atoms or so. The Li_8 OPTET cluster involves a complete filling of the first two γ -brass shells and consists of a central tetrahedron with four capping atoms, making a total of five tetrahedra. Incidentally, this Li_8 cluster is a serious violator of rule δ (edge-sharing); its electronic structure consists of four doubly-occupied tetrahedra (the central tetrahedron is empty), each sharing three edges with adjacent doubly-occupied tetrahedra (six infractions against rule δ). As a consequence, each of these four bond pairs consists of one orbital localized on a bond midpoint and one orbital localized on a face, for a net overlap of ≈ 0.67 , significantly smaller than the 0.74–0.78 overlap for typical (rule-abiding) doubly occupied tetrahedra. The first three γ -brass shells are complete at 14 atoms, leading to the γ -(4,4,6), T_d Li_{14} structure with 17 tetrahedra. By applying the rules to this Li_{14} cluster, we predict an electronic structure consisting of a doubly occupied central tetrahedron and six pairs of face-sharing singly occupied tetrahedra along the six edges of the central tetrahedron. Thus, this Li_{14} cluster may be quite stable, although it does result in four infractions against rule ϵ . The lowest energy Li_{13}^+ cluster is derived from this Li_{14} cluster by removing one atom from the outer shell and the two electrons occupying the face-shared tetrahedral pair formed by that atom.

Larger OPTET clusters are constructed by adding atoms to concave surface sites of the smaller OPTET clusters, forming at least two new tetrahedra for each atom added. For larger OPTET clusters, the number of tetrahedra shared by a given atom tends to increase as the ratio of empty to occupied tetrahedra increases. Eventually, the clusters reach sufficient size such that none of the

rules are broken. Several low-lying OPTET isomers may be competitive for any given size of cluster. The fourth and fifth γ -brass shells contain 12 atoms each, leading to a M_{26} cluster with 57 tetrahedra [γ -(4,4,6,12), T_d] and a M_{38} cluster with 97 tetrahedra. [γ -(4,4,6,12,12), T_d]. Each of the four first-shell atoms of the M_{26} cluster has full icosahedral coordination. In the M_{38} cluster, all eight atoms in the first two γ -brass shells have full icosahedral coordination.

The OPTET clusters generally lead to local fivefold symmetry axes, a result that arises from the efficient packing of tetrahedral hollows. Thus, a strict adherence to forming near perfect tetrahedra is inconsistent with 3D space groups but could play an important role in stabilization of amorphous structures.⁷ However, allowing major distortions to a small fraction of the tetrahedra can lead to periodic structures. For example, the γ -(4,4,6,12), T_d cluster of Li_{26} is isostructural with the 26-atom $Zn_4Cu_4Cu_6Zn_{12}$ cluster forming the basic motif of γ -brass (Cu_3Zn_8).⁴² These 26-atom clusters are centered at bcc lattice positions to form the γ -brass bulk structure. Thus, bulk γ -brass (Cu_3Zn_8) contains numerous fairly regular tetrahedra and relatively few severely distorted tetrahedra. In addition, many other alloy structures involve rather complicated networks of tetrahedra, e.g., the Frank–Kasper alloys^{43,44} and the Laves phases.⁴³ Thus, the rules of section IVB should provide a basis for a better understanding of the electronic structures of many alloys.

The limiting values (as $n \rightarrow \infty$) for the number of bulk sites per atom are one bond midpoint per atom for 1D, two triangular hollows per atom for planar close-packed, no more than five tetrahedral hollows per atom for OPTET, two tetrahedra per atom (and one octahedron per atom) for hcp or fcc, and six quasi-tetrahedra per atom for bcc. The quasi-tetrahedra for bcc each have four edges of normal length and two edges that are 15% longer in length. Perfect tetrahedra (with six edges of equal length) alone cannot be packed into a bulk structure without involving significant distortions (strain). Thus, for very large clusters, structures consistent with periodicity (hcp, fcc, bcc) eventually dominate.

D. GVB Descriptions of Bulk Metals. The previous discussions show that the optimum intermediate-sized clusters are *not* the most symmetric ones but that the stable structures can be predicted by using basic principles. These principles are summarized by a set of rules given in section IVB. Here, we apply these rules to close-packed (hcp and fcc) bulk elemental metals. In section IVE we present a simple rationalization of some dramatic trends in solid solubilities of alloys.

Close-packed (cp) systems have twice as many tetrahedra as atoms. In fcc, each tetrahedron shares edges with six other tetrahedra, whereas in hcp, each tetrahedron shares one face with another tetrahedron and edges with three other tetrahedra.

For a cp alkali or noble metal, only half the tetrahedra need be occupied by electrons, making the cp metals far more stable than the small cp clusters (where all tetrahedra are occupied, some with two electrons). With half the tetrahedral sites empty, these extended systems are excellent conductors.

The Be and Zn columns, with two *valence sp* electrons per atom, have one electron per tetrahedron. Thus, the GVB model suggests that the optimum electronic structure be visualized in terms of one valence electron per tetrahedron. This is consistent with an *experimental wave function* for hcp beryllium metal derived from coherent X-ray diffraction data, where it is concluded that “charge flows into the tetrahedral hole regions and out of the nuclear regions and octahedral channels.”⁴⁵ For the perfect crystal all sites are filled, leading to a semimetal. The conductivity is expected to be very sensitive to vacancies and the number of electrons on impurity atoms (hole conductor for group I (group 1),⁵⁵ normal

(42) Taylor, A. *X-Ray Metallography*; Wiley: New York, 1961.

(43) Hume-Rothery, W.; Raynor, G. V. *The Structure of Metals and Alloys*, 4th ed.; Institute of Metals: London, 1962.

(44) Frank, F. C.; Kasper, J. S. *Acta Crystallogr.* **1959**, *12*, 483. **1958**, *11*, 184.

(45) Massa, L.; Goldberg, M.; Frishberg, C.; Boehme, R. F.; La Placa, S. *J. Phys. Rev. Lett.* **1985**, *55*, 622.

conductor for group III (group 13)). Our rules do not predict which cp structure is favored for systems with two or less valence sp electrons per atom. The differences in energy between the hcp and fcc forms for these systems could involve more subtle longer range interactions. Indeed, the alkali metals^{16,46} and the alkaline-earth metals¹⁶ seem to have nearly identical energies for hcp, fcc, and bcc. The low temperature structure of Li is currently unknown, but believed to be $\approx 75\%$ close-packed rhombohedral 9R (abcbcab stacking of the planar close-packed layers; hcp has aba stacking and fcc has abc stacking) and $\approx 25\%$ bcc.⁴⁶ The noble metals (Cu, Ag, and Au) are all fcc while Zn and Cd are hcp.¹⁶

For cp systems with three valence sp electrons per atom, half the tetrahedra must be doubly occupied, while the other half are singly occupied. For both hcp and fcc it is possible to arrange the occupations so that adjacent tetrahedra are not both doubly occupied (satisfying rule δ). In this arrangement, each pair of adjacent tetrahedra contains three electrons. However, the hcp structure contains adjacent face-sharing tetrahedral pairs, while the fcc structure contains only edge-sharing tetrahedral pairs; thus, based on rule γ , we conclude that fcc should be strongly favored over hcp for group III (group 13). Indeed, neither B, Al, Ga, nor In leads to stable hcp structures, while Al leads to fcc and In to a slightly distorted fcc. With a hole in every other tetrahedron, these systems are good conductors.

With four valence electrons per atom, all tetrahedra would be doubly occupied, strongly disfavoring either cp structure (rules γ and δ). Indeed, except for Pb, the group IV (group 14) elements are either nonmetals (with strong two-electron covalent bonds) or metals with low coordination numbers. It is well-known that Hg, Tl, Pb, and Bi exhibit properties suggesting that the 6s pairs are particularly stable and do not easily form the normal sp hybrids with the 6p orbitals, perhaps rationalizing the fcc form for Pb and the hcp form for Tl.

E. Solid Solubilities. Rules δ and γ place upper limits of $2e^-/\text{atom}$ for hcp structures and $3e^-/\text{atom}$ for fcc. These limits are consistent with known alloy formations and maximum solid solubility limits.^{43,47} Thus, comparing atoms with similar sizes [Ag ($1e^-$), Zn ($2e^-$), Al ($3e^-$), and Sn ($4e^-$) with metallic radii¹⁶ of 1.44, 1.39, 1.43, and 1.54 Å, respectively], Ag and Zn are both highly soluble in fcc Al [23.8 and 66.5 at. % (atomic percent), respectively] while the solubility of Sn in Al is only 0.02 at. %. Similarly, the solubilities of Al and Sn in hcp Zn are small (2.4 and $\approx 0.10 \pm 0.04$ at. %, respectively) while Ag-Zn alloys form hcp phases with up to 33 at. % Ag (Ag₁Zn₂). The $3e^-/\text{atom}$ limit does not restrict solubilities in fcc Ag ($1e^-/\text{atom}$); hence, the solubilities are all high (Zn, 40.2 at. %; Al, 20.34 at. %; Sn, 11.5 at. %).

The fact that the maximum solubility limits of Sn in Al and of Sn or Al in Zn are very small (and not zero) is not necessarily a result of a slight violation of the rules. These solubilities may depend crucially on imperfections of the substrate (e.g., stacking faults, vacancies, dislocations, impurities, etc.). The solute atoms may tend to migrate to dislocations, surfaces, or polycrystalline grain boundaries and may actually lead to the creation of a higher density of such defects than present in the pure metal at the same temperature. For Al in Zn, the maximum solubility (2.4 at. % at 655 K or $0.94T_m$ where T_m is the melting temperature) decreases to 1.2 at. % at $0.76T_m$ and 0.15 at. % at $0.43T_m$. Thus, at lower temperatures (fewer vacancies), the limits of such solubility decrease. There are substantial disagreements among the various experiments regarding the exact values of the solubilities for Sn in Zn. Three different experiments regarding the solubility of Sn in Zn range from too small to measure (0.0 at. %) to slightly greater than 0.06 at. % (at $0.97T_m$; somewhat greater than 0.03

at. % at $0.43T_m$) to less than 0.14 at. % (presumably near T_m). The solubility of Sn in Al reaches its maximum of 0.02 at. % at $0.96T_m$, diminishes to 0.009 at. % at $0.86T_m$, and is negligibly small at $0.47T_m$. Indeed, the solubilities seem to vanish as the temperature is lowered for each of these three cases. Presumably, the density of defects similarly decreases with decreasing temperature. In contrast, for cases where the solid solubilities are high, the solubilities tend to decrease somewhat with increasing temperature but often reach sizable limits as the temperature approaches absolute zero (these systems are presumably metastable).

Here we have focused on global electron/atom trends. Of course, certain binary combinations might lead to local electronic structures that would further restrict solubility. For example, Ag_{1-x}Sn_x is hcp for $0.118 \leq x \leq 0.246$ and a slightly distorted hcp for $0.237 \leq x \leq 0.25$. The $2e^-/\text{atom}$ limit applied to hcp Ag_{1-x}Sn_x leads to the restriction $x \leq 0.33\bar{3}$, which is somewhat less restrictive than the experimental limit of $x \leq 0.25$ ($1.75 e^-/\text{atom}$). Similarly, the $2e^-/\text{atom}$ limit applied to hcp Ag_{1-x}Al_x leads to the restriction $x \leq 0.50$. This is in agreement with the experimental limits of $0.23 \leq x \leq 0.42$ for hcp Ag_{1-x}Al_x.

F. Force Fields. Fully correlated ab initio GVB calculations of the quality described herein are currently limited to a relatively small number of atoms (less than 100). This is a severe limitation since many phenomena in metallic systems would require thousands of atoms for a proper description. In order to extend our studies to such large systems, we have been using our cluster results to develop force fields that could be used in both static and dynamical simulations.³⁴ We find that, because of the special interstitial nature of the bonding, these force fields should not be described merely in terms of nuclear positions but must also involve the positions of the localized (correlated) electrons. Thus, the force field must involve both nuclear and electronic coordinates. These force fields involve such three-body terms as atom-electron-atom bend and atom-electron-atom asymmetric stretch, etc. Although still under investigation, we believe that such force fields will allow an accurate description of metallic systems that will permit reliable simulations for large systems.

V. Summary

Results of generalized valence bond studies for a variety Li₁₃⁺ geometries lead to a set of rules based on the paradigm of electrons localized in tetrahedral hollows. These rules lead to predictions of structure [e.g., the "zig-zag" clusters for M_n, $n \lesssim 8$ and the "OPTET" clusters for M_n, $8 \leq n \leq 40$] and to new rationalizations of solid solubility limits involving close-packed bulk metals. We expect that these rules apply to the valence sp electrons of a variety of structures for pure metals and for alloys, including fcc, hcp, γ -brass,^{42,43} the Laves phases,⁴³ and Frank-Kasper alloys.^{43,44} The present rules may require modification for metallic structures that possess severely distorted tetrahedra (e.g., body-centered cubic) and for structures that contain too few tetrahedra to accommodate all of the valence sp electrons (e.g., rule ζ).

The interstitial localization of the valence electrons suggests a new approach to force fields for describing metallic systems where terms involving both electronic and nuclear positions are included. Such force fields should allow simulation of the GVB wave functions for systems containing thousands of metal atoms.

The rules in combination with the force field should form a useful starting point in developing valence bond ideas for predicting geometries, electronic structure, and properties of metallic clusters, and for describing localized phenomena in solids, such as defects interfaces, or chemisorbed species. This should provide useful conceptual ideas for predicting the chemistry and catalytic properties of such systems.

Acknowledgment. This work was partially supported by grants from the National Science Foundation (Nos. DMR82-15650 and DMR84-21119).

Appendix A. Calculational Details

In this Appendix we describe various details concerning the calculations. The results presented in the previous sections of this

(46) Overhauser, R. W. *Phys. Rev. Lett.* **1984**, 53, 64. Takemura, K.; Syassen, K. *Phys. Rev. B* **1983**, 28, 1193. Anderson, M. S.; Swenson, C. A. *Phys. Rev. B* **1985**, 31, 668.

(47) Hansen, M. *Constitution of Binary Alloys*; McGraw-Hill: New York, 1958, and supplements by Elliot, R. P. (1965), Shunk, F. A. (1969), and Moffatt, W. G. (1983). Also see reviews in *Bull. Alloy Phase Diagrams*, 1980-1986.

communication stem from the usual generalized valence bond (GVB) self-consistent field^{2,48-51} and configuration interaction (CI)⁵² methods as described in the various sections of this Appendix. For comparison, this Appendix also includes results obtained from unrestricted (spin-polarized) Hartree-Fock (UHF) and restricted (nonspin-polarized) Hartree-Fock (HF). Section A.1 describes a series of studies with various basis sets. The results described in the previous sections are derived from all-electron ab initio wave functions using basis set D and are discussed in more detail in section A.3. A series of studies for the three high-symmetry clusters is presented in section A.2. Further details of the various wave functions are discussed in sections A.4 and A.5.

A.1. Basis Sets. As an initial test for the basis sets, we calculated equilibrium bond lengths (R_e), force constants (k_e), bond energies (D_e), and total energies (E_e) for both Li_2^+ and linear Li_3^+ . These cases (Li_2^+ and linear Li_3^+) were chosen because the bonding is similar to that of Li_{13}^+ . Thus, in all cases the lowest energy many-electron states are described by valence orbitals localized in interstitial regions. The results are given in Table III.

Basis sets A-G all share the same 3s Dunning⁵³ valence double- ζ (VDZ) contraction of the 9s Huzinaga⁵⁴ Gaussian-type orbital (GTO) s basis. These bases differ only in the choice of p basis and d basis (see Table IV).

Bases B, E, F, and G all entail variations of the Dunning (4p) GTO p basis (derived from the ${}^2\text{P}$ Li 1s²2p¹ atomic state). These four sets of p GTO are contracted into a single set of functions (minimum basis set, MBS) in basis set B, and they are contracted double- ζ (DZ) in bases E, F, and G. In addition, the p basis is scaled by a factor of 1.1 for basis sets F and G. The scale factor ($\zeta = 1.10$) is near optimal (with respect to the total energy) for Li_2^+ ($\zeta_{\text{opt}} = 1.114$) and for Li_3^+ ($\zeta_{\text{opt}} = 1.111$) calculated at bond length $R = 3.14 \text{ \AA}$. Basis set G also includes a single set of d GTO's optimized for Li_2^+ at $R = 3.14 \text{ \AA}$ ($\alpha_{\text{opt}} = 0.13$).

Basis set C contains a single set of p GTO's with an exponent $\alpha = 0.10$. This p exponent ($\alpha = 0.10$) is near optimum for Li_2^+ ($\alpha_{\text{opt}} = 0.110$ at $R = 3.1 \text{ \AA}$, $\alpha_{\text{opt}} = 0.106$ at $R = 3.24 \text{ \AA}$), for rhombic Li_4 ($\alpha_{\text{opt}} = 0.102$ at $R = 3.064 \text{ \AA}$, $\theta = 60^\circ$), and for Li_8 ($\alpha_{\text{opt}} = 0.113$ at $R = 3.1 \text{ \AA}$, tetracapped tetrahedron). These GTO p exponents are considerably tighter than that optimized for the ${}^2\text{P}$ Li (1s²2p¹) excited state atom ($\alpha_{2p} = 0.0466$). The exponent $\alpha = 0.10$ corresponds to scaling α_{2p} by a factor $\zeta = 1.46$.

Basis set D contains two sets of p GTO contracted MBS (2p/1p) into a single set of Slater-like functions. This is accomplished by starting with the optimum two-Gaussian basis⁵⁴ for the 2p state of H and scaling the orbital exponents while holding the contraction ratio fixed ($d_2/d_1 = 2.411792$). Note that the Li 2p atomic state is very similar to the H 2p state since the Li nucleus (3+) is effectively shielded by the Li 1s² core electrons for this state. The scale factor ($\zeta = 1.5$) was optimized for Li_2^+ at $R = 3.19 \text{ \AA}$.

(48) Hunt, W. J.; Hay, P. J.; Goddard III, W. A. *J. Chem. Phys.* **1972**, *57*, 738.

(49) Bobrowicz, F. W.; Goddard III, W. A. In *Modern Theoretical Chemistry: Methods of Electronic Structure Theory*, Schaefer III, H. F., Ed.; Plenum: New York, 1977; Vol. III, Chapter 4.

(50) Bair, R. A.; Goddard III, W. A.; Voter, A. F.; Rappé, A. K.; Yaffe, L. G.; Bobrowicz, F. W.; Wadt, W. R.; Hay, P. J.; Hunt, W. J. GVB2PS program, unpublished. See Bair, R. A. Ph.D. Thesis, California Institute of Technology, 1980, and ref 48.

(51) Yaffe, L. G.; Goddard III, W. A. *Phys. Rev. A* **1976**, *13*, 1682. Goodgame, M. M. Ph.D. Thesis, California Institute of Technology, 1984.

(52) Hay, P. J.; Dunning, Jr., T. H.; Goddard III, W. A. *J. Chem. Phys.* **1975**, *62*, 3912.

(53) Dunning, Jr., T. H.; Hay, P. J. In *Modern Theoretical Chemistry: Methods of Electronic Structure Theory*, Schaefer III, H. F., Ed.; Plenum: New York, 1977; Vol. III, Chapter 1.

(54) Huzinaga, S. *J. Chem. Phys.* **1965**, *42*, 1293.

(55) In this paper the periodic group notation (in parentheses) is in accord with recent actions by IUPAC and ACS nomenclature committees. A and B notation is eliminated because of wide confusion. Groups IA and IIA become groups 1 and 2. The d-transition elements comprise groups 3 through 12, and the p-block elements comprise groups 13 through 18. (Note that the former Roman number designation is preserved in the last digit of the new numbering: e.g., III \rightarrow 3 and 13.)

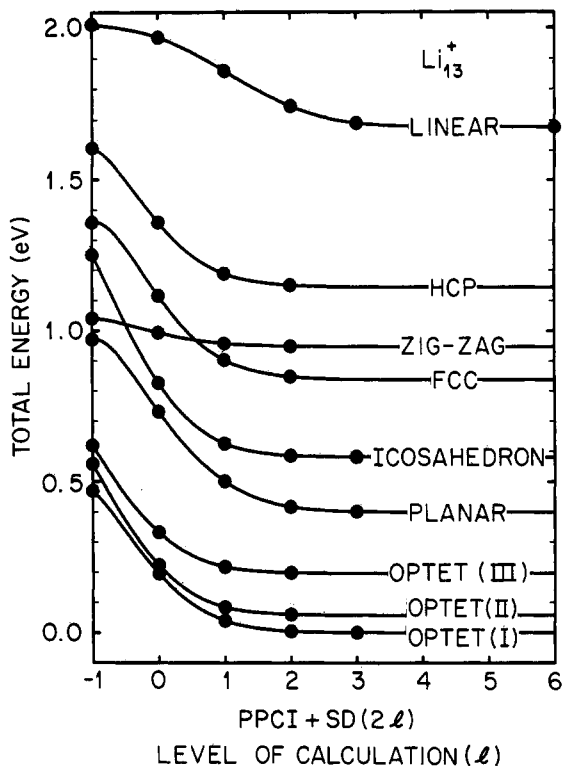


Figure 21. Total energies for nine Li_{13}^+ clusters for the PPCI+SD($2l$) wave functions as a function of l . Total energies are shown relative to the PPCI+SD(12) total energy of OPTET(I).

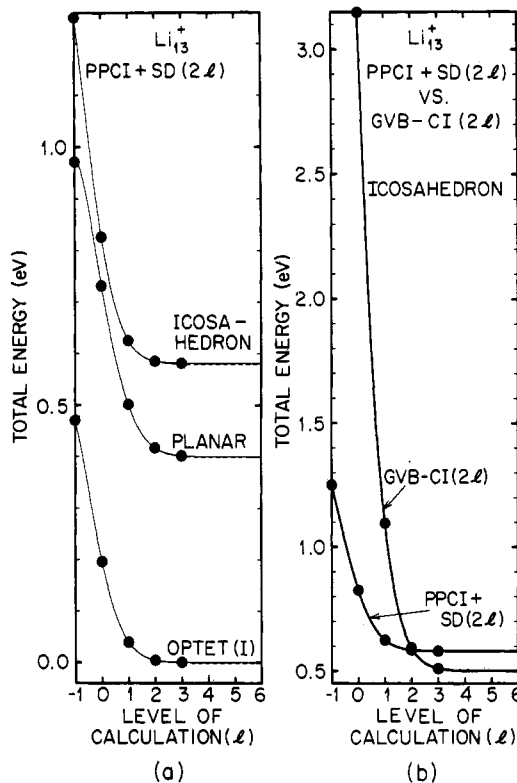


Figure 22. (a) Total energies for the OPTET(I), I_h , and planar Li_{13}^+ clusters for the PPCI+SD($2l$) wave functions as a function of l [relative to the PPCI+SD(12) total energy of OPTET(I)]. The solid lines show the extrapolations to $l = 6$ using $l = -1, 0, 1, 2$, and 3. The dashed lines show the extrapolations to $l = 6$ using $l = -1, 0, 1$, and 2. The difference in total energy for the two extrapolations is 1.6 meV for OPTET(I), 0.9 meV for I_h , and 2.0 meV for the planar cluster. (b) Total energies of the I_h Li_{13}^+ cluster for the PPCI+SD($2l$) and the GVBCI($2l$) truncations of the full GVBCI as a function of l [relative to the PPCI+SD(12) total energy of OPTET(I)]. The difference in the extrapolated energies for PPCI+SD(12) and GVBCI(12) is 0.080 eV.

TABLE III: Basis Set Comparison for $\text{Li}_2^+(^2\Sigma_g^+)$ and for Linear $\text{Li}_3^+(^1\Sigma_g^+)$;^f Basis Sets C and D Were Selected for Studies of the Li_{13}^+ Systems

basis set ^a	scale factor (p basis)	R_e , Å	k_e , eV Å ⁻²	D_e , ^b eV	E_e , hartree
Li_2^+					
A (9s,0p,0d)/(3s,0p,0d)		3.377	0.458	0.543	-14.687 68
B (9s,4p,0d)/(3s,1p,0d)	1.0	3.286	0.718	1.070	-14.707 05
C (9s,1p,0d)/(3s,1p,0d)	1.46	3.195	0.918	1.182	-14.711 16
D (9s,2p,0d)/(3s,1p,0d)	1.5	3.152	0.951	1.206	-14.712 05
E (9s,4p,0d)/(3s,2p,0d)	1.0	3.181	0.901	1.225	-14.712 75
F (9s,4p,0d)/(3s,2p,0d)	1.1	3.141	0.945	1.236	-14.713 15
G (9s,4p,1d)/(3s,2p,1d)	1.1	3.146	0.890	1.274	-14.714 53
STO 5s,5p,3d ^d		3.127	0.883	1.280	-14.716 18
experiment ^e		3.133 (13)	0.888 (10)	1.2980 (7)	
Li_3^+					
A (9s,0p,0d)/(3s,0p,0d)		3.126	1.225	0.493	-22.137 53
C (9s,1p,0d)/(3s,1p,0d)	1.46	3.149	1.760	0.804	-22.172 45
D (9s,2p,0d)/(3s,1p,0d)	1.5	3.113	1.782	0.808	-22.173 46
E (9s,4p,0d)/(3s,2p,0d)	1.0	3.140	1.705	0.830	-22.174 99
F (9s,4p,0d)/(3s,2p,0d)	1.1	3.115	1.754	0.830	-22.175 40
G (9s,4p,1d)/(3s,2p,1d)	1.1	3.123	1.670	0.856	-22.177 71

^a All wave functions are full GVB. Li_2^+ is a one-valence electron system, so that GVB and HF are equivalent. Since Li_3^+ is a two-valence electron system, GVB-PP and GVB-CI are equivalent. ^bThe dissociation limits are $\text{Li}_2^+ \rightarrow \text{Li} + \text{Li}^+$ and $\text{Li}_3^+ \rightarrow \text{Li} + \text{Li}_2^+$. ^c1 hartree = 27.21161 eV. ^dResults using a large Slater-type orbital (STO) basis set, ref 12. The $\text{Li} + \text{Li}^+$ asymptote for this basis set is lower than that for Bases A-G by 0.00142 hartree. This is due to a better description of the 1s² core electrons with the STO basis set. ^eResults obtained by extrapolating several Rydberg series of Li_2 , ref 13. Numbers in parentheses indicate the experimental uncertainty in the last digit. ^f R_e is the bond distance, k_e the force constant, D_e the bond energy, and E_e the total energy.

TABLE IV: p Bases Contractions Used in Various Calculations^a

basis set	exponent α_i	contraction coefficient d_i
A (no p functions)		
B	1.488	0.038 770
	0.266 7	0.236 257
	0.072 01	0.830 448
	0.023 70	0.817 656
C	0.10	
D	0.313 371	0.325 652
	0.072 882	0.785 405
E	1.488	0.038 770
	0.266 7	0.236 257
	0.072 01	0.830 448
	0.023 70	
F, G ^b	1.800 48	0.038 770
	0.322 707	0.236 257
	0.087 1321	0.830 448
	0.028 6770	

^aThe results of test calculations on Li_2^+ and linear Li_3^+ using these basis sets are given in Table III. In this study, basis set F was used in all Li_n calculations for $n \leq 10$ unless otherwise stated. Basis sets C or D were used in all calculations for $n > 10$. ^bBasis set G also includes a set of d GTO's with exponent $\alpha = 0.13$.

The overall trends of differences in the calculated results (Table III) among the various bases are very similar for both Li_2^+ and linear Li_3^+ . The various bases are listed in order of increasing overall quality, as determined by the variational principle (decreasing total energy). The Li_2^+ results calculated with basis set G are in reasonable agreement with results calculated with a large Slater-type orbital (STO) basis¹² and with experiment.¹³

The importance of p and d polarization functions is indicated from a comparison of the results for bases A, F, and G. For Li_2^+ , the p_z functions and d_{z^2} functions contribute 54.4% and 3.0%, respectively, of the total bond energy (of basis set G).

Comparing MBS p-basis results (bases B, C, and D) indicates that the optimum p function for bonding is much more compact ($\zeta \approx 1.5$) than the Li 2p atomic function ($\zeta = 1.0$). [The optimum scale factor for the DZ p basis ($\zeta = 1.1$; F,G) is smaller because of the added flexibility of the DZ basis.] Scaling the p basis ($\zeta > 1.0$) results in a decrease in the calculated R_e and an increase in the calculated k_e .

These results indicate that bases C and D should be reasonably accurate for cluster calculations. Calculations with bases E, F, and G generally result in increases in the computation time by factors of at least 5, 5, and 40, respectively. We have employed basis set E in the calculations presented here for all clusters of ten atoms or less. For these cases, the GVB results refer to untruncated GVB-CI wave functions (full CI within the valence

TABLE V: Optimum Geometries for the High-Symmetry Li_{13}^+ Clusters^c

structure	basis set C			basis set D ^a		
	R_e ^b , Å	k_e , eV Å ⁻²	E_e , hartree	ΔE_e , eV	E_e , hartree	ΔE_e , eV
GVB-PP ^c						
icosahedron	3.241	15.0	-96.673 71	0.00	-96.687 83	0.00
fcc	3.239	12.9	-96.667 10	0.18	-96.683 88	0.11
hcp	3.244	13.3	-96.659 26	0.39	-96.674 77	0.36
PPCI+SD(0) ^d						
icosahedron	3.234	15.1	-96.688 25	0.00	-96.703 44	0.00
fcc	3.245	12.7	-96.676 66	0.32	-96.692 81	0.29
hcp	3.228	13.4	-96.667 70	0.56	-96.683 89	0.53
PPCI+SD(2) ^d						
icosahedron	3.230	15.2	-96.695 69	0.00	-96.710 84	0.00
fcc	3.243	12.6	-96.684 33	0.31	-96.700 64	0.28
hcp	3.222	13.5	-96.673 78	0.60	-96.690 14	0.56

^aCalculated at $R_e^{\text{RMS}} = 3.19$ Å (see section A.1). ^b $R_e^{\text{RMS}} = R_e^{\text{BS}} = R_e^{\text{SS}}$ for the fcc and hcp clusters. For the icosahedron, $R_e^{\text{BS}} = 0.964 R_e^{\text{RMS}}$; $R_e^{\text{SS}} = 1.014 R_e^{\text{RMS}}$. ^cGVB-PP is a 64-configuration MCSCF wave function that allows an independent particle description. ^dThe full 73 789-configuration GVBCI was truncated to PPCI+SD(0), 535 configurations, and PPCI+SD(2), 2875 configurations (see section A.4). ^e R_e^{RMS} is the average bond distance, k_e the force constant, E_e the total energy, ΔE the relative energy.

TABLE VI: Relative Total Energies (eV) for Li_{13}^+ Clusters (Basis Set D)

structure ^a	HF ^b	UHF ^c	GVB-PP ^d	PPCI+SD(2 <i>l</i>) ^{e,f}				
				<i>l</i> = 0	<i>l</i> = 1	<i>l</i> = 2	<i>l</i> = 3	<i>l</i> = 6
OPTET(I) ^g	0.00	0.00	0.00	0.00	0.00	0.00	0.00	0.00
OPTET(II) ^g	-0.29	0.10	0.09	0.03	0.04	0.06	0.06	0.06
OPTET(III) ^g	-0.03	0.10	0.15	0.14	0.18	0.19	0.20	0.20
planar	1.13	0.03	0.50	0.54	0.46	0.41	0.40	0.40
icosahedron	0.75	0.18	0.78	0.63	0.59	0.58	0.58	0.58
fcc	0.98	0.32	0.89	0.92	0.86	0.84	0.84	0.84
zig-zag chain	0.88	1.27	0.57	0.80	0.92	0.94	0.95	0.95
hcp	1.02	0.53	1.14	1.16	1.15	1.15	1.14	1.14
linear chain	4.70	0.84	1.54	1.77	1.82	1.74	1.69	1.68
correlation ^h	0.00	0.93	1.77	2.04	2.20	2.23	2.24	2.24

^aThe structures are shown in Figures 11, 15–17, 19, and 20. $R^{\text{RMS}} = 3.19 \text{ \AA}$ except for the linear chain ($R^{\text{RMS}} = 3.12 \text{ \AA}$) and for the zig-zag chain ($R^{\text{RMS}} = 3.12 \text{ \AA}$, $\theta = 70^\circ$). ^bThe HF wave function (closed shell) contains only one configuration (one determinant). The orbitals were optimized with spin restrictions but without spacial (symmetry) restrictions. ^cThe UHF wave function ($M_S = 0$) contains only one configuration (one determinant). The orbitals were optimized without any restrictions (spin or spacial). ^dThe GVB-PP wave function contains 64 configurations in the natural orbital representation, but leads only one configuration (64 spin determinants) in the GVB single particle representation. The orbitals were optimized with the usual strong-orthogonality and PP restrictions. The GVB-PP and PPCI ($l = -1$) total energies are almost identical. The largest difference in total energy for these two wave functions is for the OPTET(I) cluster (0.0035 eV). ^eThe PPCI+SD(0), PPCI+SD(2), PPCI+SD(4), PPCI+SD(6), and PPCI+SD(12) wave functions [535, 2875, 7615, 12595 and 16336 configurations, respectively] are truncations of the full GVB-CI wave function [73789 configurations]. The GVB-CI wave function overcomes the strong orthogonality and PP restrictions of GVB-PP. ^fThe $l = 3$ and $l = 6$ total energies were obtained by extrapolating the PPCI+SD(2*l*) total energies as a function of *l* as shown in Figures 21 and 22, except for the following cases where the total energies were calculated exactly. $l = 3$: OPTET(I), planar icosahedron and linear chain; $l = 6$: linear chain. ^gThe low symmetry clusters generated from rules α through ζ ; see Figure 19. ^hThe electron correlation energy of the OPTET(I) cluster is listed for each wave function. The correlation energy for each wave function is defined as the difference between the total energy calculated with that wave function and the HF total energy (-96.65158 hartree).

TABLE VII: Cartesian Coordinates for the Li_{13}^+ OPTET Clusters ^a

atom(s)	x, Å	y, Å	z, Å
OPTET(I), $\rho = 0.071 \text{ \AA}$			
1, 2	0.00000	±1.59347	1.12755
3, 4	±1.56394	0.00000	-1.17928
5, 6	±2.61908	0.00000	1.83800
7, 8	0.00000	±2.73547	-1.76769
9, 10, 11, 12	±2.72811	±2.67928	0.00000
13	0.00000	0.00000	3.81622
OPTET(II), $\rho = 0.059 \text{ \AA}$			
1	0.00000	-1.60050	1.08096
2	0.00000	1.48229	1.12596
3, 4	±1.56928	0.00000	-1.25332
5, 6	±2.75071	-0.02611	1.65063
7	0.00000	-2.72096	-1.85973
8	0.00000	2.68811	-1.85632
9, 10	±2.70953	-2.72483	-0.11260
11, 12	±2.60753	2.76503	0.00000
13	0.00000	4.59190	0.65458
OPTET(III), $\rho = 0.070 \text{ \AA}$			
1	0.00000	0.00000	-0.20716
2, 3	0.00000	±2.87994	-1.47451
4, 5, 6, 7	±2.61325	±1.64063	0.00000
8, 9	0.00000	±2.57908	1.66727
10, 11	±1.61648	0.00000	2.53828
12, 13	0.00000	±1.61004	4.73812

^a $R^{\text{RMS}} = 3.19 \text{ \AA}$; ρ is the root mean square deviation of R^{RMS} . The OPTET clusters are shown in Figure 19.

orbitals) where the orbitals have been optimized at the GVB-CI level. The calculations on the Li_{10} ring cluster are described in greater detail elsewhere.⁵ The calculations on Li_{13}^+ employ bases C or D and are described in further detail in the subsequent sections of this Appendix.

A.2. High-Symmetry Li_{13}^+ Clusters. The I_h , fcc, and hcp clusters (Figures 15–17) each consist of a central “bulk” atom surrounded by 12 surface atoms equidistant from the bulk atom. We performed calculations for several internuclear separations (R^{BS}) between the bulk and surface atoms and interpolated the results to obtain equilibrium values (R_e^{BS}). Results at the perfect-pairing GVB (GVB-PP)⁴⁸ and configuration interaction GVB (GVB-CI) levels are shown in Table V. Details of the GVB-PP and various truncated GVB-CI wave functions [PPCI+SD(0), PPCI+SD(2), etc.] are given in sections A.4 and A.5. The

GVB-CI wave function allows a less-restricted treatment of the electron correlation than the GVB-PP wave function. Consequently, the GVB-CI leads to slightly lower total energies (≈ 0.44 eV) and slightly smaller bond lengths ($\approx 0.009 \text{ \AA}$) in comparison to GVB-PP.

For the icosahedron, R^{BS} is 4.9% smaller than the surface-surface bond distance (R^{SS}). In order to compare bond lengths of different structures, we use the root mean square distance (R^{RMS}). For the fcc and hcp structures $R^{\text{RMS}} = R^{\text{BS}} = R^{\text{SS}}$, whereas for the I_h structure, $R^{\text{RMS}} = 0.986 R^{\text{SS}} = 1.037 R^{\text{BS}}$. The validity of R^{RMS} as a measure of size is indicated by the close correspondences: $R_e^{\text{RMS}}(I_h) = 3.230 \text{ \AA}$, $R_e^{\text{RMS}}(\text{fcc}) = 3.243 \text{ \AA}$, and $R_e^{\text{RMS}}(\text{hcp}) = 3.222 \text{ \AA}$.

For the hcp cluster we fixed the c/a ratio⁴³ at 1.633 so that all the nearest-neighbor distances are equal. Thus, the fcc and hcp clusters both have the same number of bulk-surface and surface-surface nearest neighbors. Even so, hcp leads to a bond distance 0.02 Å smaller than fcc.

Optimum bond lengths (R_e^{RMS}), force constants, total energies, and relative energies (ΔE_e) were calculated for the I_h , fcc, and hcp clusters by using basis set C. Since the energy differences among these three high-symmetry Li_{13}^+ are rather small (≈ 21 meV/atom), we also carried out calculations using a slightly better p basis (basis set D). We did not optimize R^{RMS} with basis set D; rather we chose $R^{\text{RMS}} = 3.19 \text{ \AA}$ based on the average of the I_h , fcc, and hcp values for basis set C ($R_e^{\text{RMS}} = 3.23 \text{ \AA}$) corrected by the difference in R_e values calculated with the two basis sets for linear Li_3^+ (0.04 Å, see Table III). The results calculated by using basis C (Table V) justify choosing a fixed R^{RMS} rather than optimizing separate values for the various clusters. Actually, the relative energies are rather insensitive to the value of R . Thus, changing R^{RMS} by as much as 0.05 Å from R_e^{RMS} would lead to errors in the total energy of less than 0.02 eV (assuming $k_e < 16.0 \text{ eV \AA}^{-2}$). The relative energies (ΔE) of basis set D compare quite favorably with those of basis set C. Thus, at the GVB-CI level [PPCI+SD(2)], the maximum difference in ΔE between the two basis sets is 0.04 eV. We have chosen basis set D and $R^{\text{RMS}} = 3.19 \text{ \AA}$ for the lower symmetry clusters (to avoid the expense of further geometry optimizations). Since the total energies for basis set D are slightly lower [≈ 0.015 hartree] than those for basis set C, the ΔE values from basis set D are expected to be somewhat more reliable than those from basis set C.

A.3. Results for Li_{13}^+ Clusters Using Basis Set D. Total energies (E) of nine Li_{13}^+ structures are given in Table VI for

TABLE VIII: Truncated GVB-CI Results for the Li_{13}^+ Icosahedron

wave function ^a	E , hartree	truncation ^b error, mhartree	size of CI wave function			CPU time, ^c h
			SC	SEF	DET	
PPCI	-96.687834	24.639	64	64	64	0.00
PPCI+SD(0)	-96.703443	9.029	535	760	1876	0.06
PPCI+SD(2)	-96.710836	1.636	2875	4300	11236	0.38
PPCI+SD(4)	-96.712295	0.177	7615	11680	31096	1.60
PPCI+SD(6)	-96.712457	0.015	12595	19720	53176	3.63
PPCI+SD(12)	-96.712472 ^b	0.000	16336	26176	71488	6 ^d
GVBCI(0)	-96.618059	97.344	1	1	1	0.00
GVBCI(2)	-96.693517	21.886	478	703	1819	0.00
GVBCI(4)	-96.711957	3.446	11078	28278	98694	0.23
GVBCI(6)	-96.715067	0.336	46835	147042	558810	3.50
GVBCI(12)	-96.715403 ^b	0.000	73789	226512	853776	9 ^d

^aBasis set D, $R^{\text{RMS}} = 3.19 \text{ \AA}$. ^bThe PPCI+SD(12) and GVBCI(12) energies were obtained by extrapolating the results for $2l = -2, 0, 2, 4$, and 6 to $2l = 12$ (see Figure 2). ^cMachine time required on a DEC VAX 11/780 computer. The GVBCI($2l$) calculations utilize symmetry in solving for the wave functions (D_{2h} for the Li_{13}^+ icosahedron); cases with lower symmetries would involve much more CPU time, e.g., by factors of more than 4, 16, and 64 for C_{2v} , C_s , and C_1 symmetries, respectively. ^dEstimated CPU time.

HF, unrestricted HF (UHF), GVB-PP, and various truncated GVB-CI wave functions. Details of these wave functions are given in sections A.4 and A.5.

For seven of the nine clusters we have chosen $R^{\text{RMS}} = 3.19 \text{ \AA}$ based on results given in section A.2. For the linear chain Li_{13}^+ cluster (Figure 11a) we chose $R = 3.12 \text{ \AA}$ based on $R_e = 3.143 \text{ \AA}$ for the infinite Li chain [$\text{Li}_{(1D)}$] calculated with basis set E⁵ and the 0.027- \AA correction between basis set E and basis set D (see Table III). For the zig-zag chain (Figure 11b), we chose $R = 3.12 \text{ \AA}$ and a bond angle (θ) of 70° . This bond angle ($\theta = 70^\circ$) is close to that optimized for $\Psi^{\text{GVB-PP}}$ for the Li_{13}^+ zig-zag chain ($\theta_{\text{opt}} = 70.7^\circ$ at $R = 3.12 \text{ \AA}$) and to the optimum bond angle of the planar Li_6 cluster ($\theta_{\text{opt}} = 69.8^\circ$, Figure 9b) calculated at the full GVB level.

The OPTET clusters (Figure 19) are similar to the icosahedron in that the nearest-neighbor bond lengths (or tetrahedral edge lengths) cannot all be chosen equal. For the icosahedron, the ratio $R^{\text{BS}}/R^{\text{SS}}$ is fixed by symmetry. The OPTET clusters have relatively low symmetries, thus there is considerable freedom in choosing the various bond lengths. Geometries for the OPTET clusters were obtained by minimizing the root mean square deviation (ρ) of all (N) nearest-neighbor bond lengths (R_i). Thus

$$\rho^2 = \frac{1}{N} \sum_{i=1}^N (R_i - R^{\text{RMS}})^2 \quad (8)$$

was minimized for $N = 38$ different bond lengths for each of the three OPTET clusters (each of the OPTET clusters contains 38 nearest-neighbor contacts). Obtaining the geometries in this fashion is equivalent to minimizing the strain energy, assuming equivalent harmonic bonds between each pair of nearest-neighbor atoms. Cartesian coordinates for the three OPTET clusters ($R^{\text{RMS}} = 3.19 \text{ \AA}$) are given in Table VII. Nearest-neighbor bond lengths for these clusters all lie in the range $R = 3.19 \pm 0.11 \text{ \AA}$, while next-nearest neighbors are at $R \approx 5.2 \text{ \AA}$.

It is important to include the valence electron correlation effects implicit in the GVB wave function. For the I_h cluster, we estimate that the total energy of the full (untruncated) GVB-CI wave function is -96.71540 hartree (see section A.5). In comparison, the PPCI+SD(4), GVB-PP, UHF, and HF wave functions lead to total energies that are higher than the estimated full GVB-CI total energy by 0.08, 0.75, 0.98, and 2.49 eV, respectively [1 eV = 36.74902 mhartrees].

We find that the PPCI+SD($2l$) wave functions lead to very efficient truncations of the full GVB-CI wave function and include a large fraction of the energy difference between GVB-PP and full GVB-CI (see section A.5). PPCI+SD($2l$) energies for the various Li_{13}^+ clusters are plotted as a function of l in Figure 21 [PPCI+SD(-2) \approx PPCI \approx GVB-PP] and extrapolated to $2l = n_e$ (n_e is the total number of valence electrons; $n_e = 12$ for Li_{13}^+). Since the various curves in Figure 21 do not all have exactly the same form, we have used "cubic" splines³⁴ with segments having the functional form

$$E(l) = \sum_{i=0}^3 c_i (n_e - 2l)^{4i} \quad (9)$$

to perform the various extrapolations (the power of four was found to be required in order to give accurate extrapolations). In order to test the extrapolations, we compare the extrapolated limits ($l = 6$) obtained with four points ($l = -1, 0, 1$, and 2) with those obtained with five points ($l = -1, 0, 1, 2$, and 3). Figure 22a shows the 4-point (dashed line) and 5-point (solid line) extrapolations for the OPTET(I), planar (Figure 20), and I_h clusters. The 4-point total energy limits are lower than the 5-point limits by 1.6, 0.9, and 2.0 meV for the OPTET(I), planar, and I_h clusters, respectively. The linear cluster differs from the other clusters in that the convergence of the PPCI+SD($2l$) energies with increasing l is rather slow, thus we calculated the PPCI+SD(12) energy exactly. For the linear cluster, the 4-point and 5-point $l = 6$ extrapolated limits are higher than the $l = 6$ calculated value by 37 and 3.6 meV, respectively. These results indicate that the extrapolated total energies in Table VI differ from calculated values by only negligible amounts (≈ 2 meV).

Figure 21 shows that the relative energies (ΔE_e) of the various clusters are fairly consistent for the GVB-PP and truncated GVB-CI wave functions [PPCI+SD($2l$), $l = 1, 2, 3, \dots, 6$], except for the zig-zag chain cluster. (Eliminating the zig-zag chain cluster, the GVB-PP and various PPCI+SD($2l$) wave functions all give the same ordering of the eight remaining Li_{13}^+ structures.) In comparison to the PPCI+SD(12) results, the root mean square errors in ΔE_e values for the various PPCI+SD($2l$) wave functions are 0.165, 0.089, 0.057, 0.023, and 0.004 eV for $l = -1$ (PPCI or GVB-PP), 0, 1, 2, and 3, respectively. Since the difference in *total energy* between the PPCI+SD(12) and full GVB wave functions is only ≈ 0.08 eV (see section A.5), the PPCI+SD(12) ΔE values represent a very good approximation to the full (untruncated) GVB-CI. The error in the PPCI+SD(12) ΔE values as compared with the full GVB-CI is expected to be much better than ≈ 0.08 eV due to cancellation effects.

For several cases the relative energies for HF and UHF differ substantially from those of GVB. In comparison with the PPCI+SD(12) results, the root mean square errors in ΔE for HF and UHF are 1.11 and 0.47 eV, respectively. The closed-shell HF wave function correctly predicts that, of the nine structures, the OPTET clusters are the lowest in energy and the linear chain is the highest in energy. However, HF does not predict the correct ordering of the three OPTET clusters and gives relative energies for the planar cluster and linear chain that are 0.73 and 3.02 eV too high, respectively. Although the UHF results are somewhat more reliable than the HF results, the planar and linear chain clusters are still poorly described (0.37- and 0.83-eV errors in ΔE , respectively).

A.4. Self-Consistent Field Wave Functions. Here we describe the HF, UHF, and GVB wave functions which have been solved for self-consistently; e.g., the orbitals have been optimized in such

a manner as to give the lowest possible energy (within the particular basis set) for the particular form of wave function. In general, we have allowed the orbitals to break symmetry, almost always leading to substantially lower energies than similar wave functions where symmetry restrictions are imposed on the orbitals.

For the Li_{13}^+ clusters, the Li 1s² core orbitals are optimized at the Hartree-Fock level for a suitable valence state of Li_{13}^+ and left frozen at this level and uncorrelated in subsequent calculations. The difference in total energy (E) between generalized valence bond (GVB) calculations performed in this manner and GVB calculations allowing the 1s² core orbitals to relax (but remain uncorrelated) is negligible, e.g., 0.10 mhartree for $\text{I}_h \text{Li}_{13}^+$.

The closed-shell restricted Hartree-Fock many electron wave function (Ψ^{HF}) of Li_{13}^+ is written

$$\Psi^{\text{HF}} = \hat{A}[\Phi^{\text{CORE}}\psi_1(1)\psi_1(2)\psi_2(3)\psi_2(4)\psi_3(5)\psi_3(6) \dots \psi_6(11)\psi_6(12)\chi^{\text{HF}}] \quad (10)$$

where \hat{A} is the antisymmetrizer (determinantal operator), Φ^{CORE} contains the 13 doubly occupied Li 1s core orbitals, $\{\psi_i\}$ are doubly occupied orthogonal valence orbitals, and

$$\chi^{\text{HF}} = \alpha(1)\beta(2)\alpha(3)\beta(4)\alpha(5)\beta(6)\dots\alpha(11)\beta(12)] \quad (11)$$

is the HF spin function where α and β are the electronic spin functions describing the up-spin ($m_s = +\frac{1}{2}$) and down-spin ($m_s = -\frac{1}{2}$) projections, respectively. Although it is often customary to apply symmetry restrictions to the HF orbitals when solving for their optimum shapes, this often results in higher energies than similar calculations without such spatial symmetry restrictions.⁵ Thus, we solved for the optimum (self-consistent) orbitals $\{\psi_i\}$ for Ψ^{HF} without imposing spatial symmetry restrictions.

The low-spin unrestricted Hartree-Fock many electron wave function (Ψ^{UHF}) is written

$$\Psi^{\text{UHF}} = \hat{A}[\Phi^{\text{CORE}}\varphi_{1A}\varphi_{1B}\varphi_{2A}\varphi_{2B}\varphi_{3A}\varphi_{3B}\dots\varphi_{6A}\varphi_{6B}\chi^{\text{HF}}] \quad (12)$$

where it is understood that the electronic coordinates are labeled sequentially. Again, we solved Ψ^{UHF} self-consistently without imposing spatial symmetry restrictions on the orbitals $\{\varphi_{iA}, \varphi_{iB}\}$. Making the restriction $\varphi_{iA} = \varphi_{iB}$ results in Ψ^{HF} , thus the UHF total energy is never higher than the HF total energy (Ψ^{UHF} eschews the HF restriction of doubly occupied valence orbitals). Here, singly occupied orbitals are partitioned into two sets $\{\varphi_{iA}\}$ and $\{\varphi_{iB}\}$. Because of the Pauli principle (\hat{A}), orbitals within one set are mutually orthogonal but are allowed to overlap orbitals of the other set. Although the spin projection of each electron is quantized in χ^{HF} , Ψ^{UHF} is not an exact eigenfunction of the total spin operator (\hat{S}^2) and hence does not give the correct spin spectrum of the many-electron states.⁵

The perfect-pairing GVB wave function ($\Psi^{\text{GVB-PP}}$) has the form

$$\Psi^{\text{GVB-PP}} = \hat{A}[\Phi^{\text{CORE}}(\phi_{1A}\phi_{1B})(\phi_{2A}\phi_{2B})(\phi_{3A}\phi_{3B})\dots(\phi_{6A}\phi_{6B})\chi^{\text{PP}}] \quad (13)$$

where

$$\chi^{\text{PP}} = (\alpha\beta - \beta\alpha)(\alpha\beta - \beta\alpha)(\alpha\beta - \beta\alpha)\dots(\alpha\beta - \beta\alpha) \quad (14)$$

describes a singlet spin eigenstate (of \hat{S}^2) in which singly occupied, nonorthogonal pairs of orbitals (ϕ_{iA}, ϕ_{iB}) are described as two-electron singlet spin eigenstates and solved for self-consistently (energy-optimized). For Li_{13}^+ , the optimum canonical UHF orbitals are somewhat delocalized over the cluster, while the optimum GVB-PP orbitals tend to be fairly localized. Although the GVB-PP wave function is a proper exact eigenfunction of \hat{S}^2 , the spin function χ^{PP} is not in general optimum. In $\Psi^{\text{GVB-PP}}$, the strong orthogonality⁴⁸ restriction is imposed; i.e., for Li_{13}^+ the 12 valence orbitals are partitioned into six bond pairs, and each orbital is allowed to overlap only the orbital that it is paired with (e.g., ϕ_{1A} is allowed to overlap ϕ_{1B}) but is restricted to be orthogonal to all of the other orbitals. The qualitative aspects of the electronic structure are discussed in terms of $\Psi^{\text{GVB-PP}}$ since the localized GVB-PP one-electron orbitals provide a useful conceptual description of the bonding.

The GVB-PP description is excellent for systems such as hydrocarbons or crystalline silicon in which there is only one favorable way to spin pair the orbitals on various atoms to form strong (high overlap) two-center, two-electron bonds. However, for metallic systems such as Li_{13}^+ , each localized valence orbital may have several near neighbor orbitals with which it could overlap and be spin-paired. Thus, there may be several nearly equivalent ways (resonance structures) of forming bond pairs. For such systems, it is important to allow each localized orbital to overlap all adjacent orbitals and to optimize the spin function χ (including thereby the optimum combination of bonding structures) in order to maximize the total exchange energy stabilization resulting from all of these adjacent overlaps.⁵ In order to allow for the optimum description of such resonance effects, a full GVB description is needed.

The full GVB wave function has the form

$$\Psi^{\text{GVB}} = \hat{A}[\Phi^{\text{CORE}}\phi_{1A}\phi_{2A}\phi_{3A}\dots\phi_{12}\chi^{\text{GVB}}] \quad (15)$$

with one orbital per valence electron (as in Ψ^{UHF} and $\Psi^{\text{GVB-PP}}$), but now the spin function (χ^{GVB}) and the orbitals $\{\phi_i\}$ are optimized simultaneously without restrictions.¹⁸ Thus, the valence orbitals are no longer partitioned artificially into two sets (as in UHF) or six bond pairs (as in GVB-PP). Rather, each orbital is allowed to overlap all the other orbitals. Unfortunately, Ψ^{GVB} is not practicable for N larger than eight or ten (because of the large number of overlapping terms); thus, it is customary to approximate Ψ^{GVB} by using orbitals derived from $\Psi^{\text{GVB-PP}}$ in a CI expansion (GVB-CI).⁵² A full CI over GVB orbitals also requires a large amount of computational effort for 12 electrons (especially for low symmetry cases), and consequently we have employed truncations of $\Psi^{\text{GVB-CI}}$, as described in the following section.

A.5. Truncated GVB-CI Wave Functions. The GVB-PP wave function of Li_{13}^+ involves 13 doubly occupied 1s core orbitals and 12 singly occupied valence orbitals partitioned into six bond pairs $\{(\phi_{iA}, \phi_{iB}), i = 1, 2, \dots, 6\}$. The 12 valence orbitals are optimized self-consistently for each geometry, while allowing the orbitals to localize (no symmetry restrictions are imposed) and overlap in pairs. For describing the GVB-CI, it is useful to expand the GVB (overlapping) orbitals $\{\phi_{iA}, \phi_{iB}\}$ in terms of GVB orthogonal natural orbitals^{50,52} $\{\psi_{iA}, \psi_{iB}\}$ as

$$\phi_{iA} = (\sigma_{iA}^{1/2}\psi_{iA} + \sigma_{iB}^{1/2}\psi_{iB})/(\sigma_{iA} + \sigma_{iB})^{1/2} \quad (16)$$

$$\phi_{iB} = (\sigma_{iA}^{1/2}\psi_{iA} - \sigma_{iB}^{1/2}\psi_{iB})/(\sigma_{iA} + \sigma_{iB})^{1/2} \quad (17)$$

where the expansion coefficients $\sigma_{iA} > 0, \sigma_{iB} > 0$ are related to the overlap of ϕ_{iA} and ϕ_{iB}

$$(\sigma_{iA} - \sigma_{iB})/(\sigma_{iA} + \sigma_{iB}) = \langle \phi_{iA} | \phi_{iB} \rangle \quad (18)$$

$$\sigma_{iA}^2 + \sigma_{iB}^2 = 1.0 \quad (19)$$

In this way, $\Psi^{\text{GVB-PP}}$ can be rewritten in terms of doubly occupied (natural) orbitals ($\psi_{1A}, \psi_{1B}\dots\psi_{6A}, \psi_{6B}$) as

$$\Psi^{\text{GVB-PP}} = \hat{A}[\Phi^{\text{CORE}}(\sigma_{1A}\psi_{1A}\psi_{1A} - \sigma_{1B}\psi_{1B}\psi_{1B}) \dots (\sigma_{6A}\psi_{6A}\psi_{6A} - \sigma_{6B}\psi_{6B}\psi_{6B})\chi^{\text{HF}}] \quad (20)$$

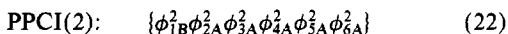
Since each of the six bond pairs involves two configurations in the natural orbital representation, this CI form of $\Psi^{\text{GVB-PP}}$ involves $2^6 = 64$ spatial configurations (SC) and one spin term (χ^{HF}). In comparison, the independent particle form of $\Psi^{\text{GVB-PP}}$ involves just one SC but 64 spin terms (in χ^{PP}). Thus, both forms of $\Psi^{\text{GVB-PP}}$ lead to 64 determinants for Li_{13}^+ .

A full (untruncated) GVB-CI (allowing all possible combinations of 12 electrons among 12 orbitals) involves 73 789 SC [226 512 spin eigenfunctions (SEF), 853 776 determinants (DET)]. Consequently, we have employed truncations of $\Psi^{\text{GVB-CI}}$.

We find that a particular set of truncations of $\Psi^{\text{GVB-CI}}$ [based on the CI form of $\Psi^{\text{GVB-PP}}$] is quite useful for Li_{13}^+ . First we partition the 64 SC of $\Psi^{\text{GVB-PP}}$ into seven sets. The "zeroth order" set consists of the single (dominant) SC with two electrons in the first natural orbital for each of the six bond pairs

$$\text{PPCI}(0): \quad \{\psi_{1A}^2\psi_{2A}^2\psi_{3A}^2\psi_{4A}^2\psi_{5A}^2\psi_{6A}^2\} \quad (21)$$

The second-order set consists of the six SC involving a double excitation in just one of the six pairs, e.g.



In general, the $2l$ -th order set [PPCI($2l$)] consists of the $\binom{6}{l}$ SC involving double excitations in l of the six bond pairs, thus the 64 SC partition as $1 + 6 + 15 + 20 + 15 + 6 + 1$ for the sets of order 0, 2, 4, 6, 8, 10, and 12, respectively.

The PPCI wave function is simply the CI wave function involving these 64 SC. Thus Ψ^{PPCI} is nearly equivalent to $\Psi^{\text{GVB-PP}}$, the only difference being the coefficient restrictions of $\Psi^{\text{GVB-PP}}$, which leads to Ψ^{PPCI} having total energies generally lower than $\Psi^{\text{GVB-PP}}$ by about 0.01 millihartree. PPCI+SD(0) is defined as the wave function consisting of PPCI plus all single and double excitations (within the GVB natural orbitals) from PPCI(0). The PPCI+SD(2) truncation is PPCI plus all single and double excitations from the seven configurations included in PPCI(0) and PPCI(2). In general, PPCI+SD($2l$) is defined as the wave function consisting of PPCI+SD($2l-2$) plus all additional single and double excitations from PPCI($2l$).

The limit of the PPCI+SD($2l$) series is PPCI+SD(n_e), where n_e is the total number of valence electrons ($n_e = 12$ for Li_{13}^+). The PPCI+SD(n_e) wave function is equivalent to PPCI times singles and doubles (PPCI×SD) and includes all excitations up to second order from all 64 SC in PPCI. For Li_{13}^+ , the PPCI wave function differs from the full GVB-CI wave function by

excitations up to sixth order, since PPCI already includes selected closed-shell excitations up to twelfth order from the dominant SC.

We find for Li_{13}^+ that the PPCI+SD($2l$) truncations of $\Psi^{\text{GVB-CI}}$ lead to an efficient method of including nearly all of the important electronic correlation effects of the full GVB-CI; e.g., PPCI+SD(12) includes $\approx 90\%$ of the total energy difference between GVB-PP and full GVCi. We tested the PPCI+SD($2l$) truncations for the I_h cluster by comparing the total energies with those calculated with the GVB-CI($2l$) truncations as described below (see Table VIII and Figure 22b).

The GVB-CI(0) wave function consists of the dominant SC of the zeroth order set. GVB-CI(2) is defined as GVB-CI(0) plus all single and double excitations from the dominant SC. In general, GVB-CI($2l$) consists of GVB-CI($2l-2$) plus $l-1$ and l order excitations from the dominant SC, thus GVB-CI(12) is the full (untruncated) GVB-CI wave function.

Results for the PPCI+SD($2l$) and GVB-CI($2l$) truncated CI wave functions are given in Table VIII and Figure 22b for $l = -1, 0, 1, 2$, and 3 and are extrapolated to $l = 6$ for the I_h cluster. Both series of truncations are fairly well converged at $l = 3$. The error in the PPCI+SD(12) total energy (compared to the estimated full GVB-CI result) is only 0.08 eV. Errors in the PPCI+SD(12) relative energies (due to truncation of the GVB-CI) are certainly much smaller (due to cancellation effects).

Registry No. Li, 7439-93-2.

Spectroscopy of Vibrational Ground-State Levels of Na_3

M. Broyer,[†] G. Delacrétaz,^{‡§} P. Labastie,[†] J. P. Wolf,[‡] and L. Wöste^{*†}

Laboratoire de Spectrométrie Ionique et Moléculaire (associé au CNRS No. 171), Université Lyon I, Bât. 205, 69622 Villeurbanne Cedex, France, and Institut de Physique Expérimentale, Ecole Polytechnique Fédérale de Lausanne, PHB-Ecublens, CH-1015 Lausanne, Switzerland (Received: June 17, 1986)

The two-photon ionization spectrum of Na_3 is recorded for various vibrational temperatures. It leads to the assignments of hot bands in the A, B, and C systems. The vibrational structure of the ground state is then deduced and compared to recent theoretical calculations.

Introduction

Despite intense activity in the field of cluster research, information about the ground-state potential surface of these particles is extremely scarce. Generally, only some binding energies have been experimentally determined so far, using methods such as the study of equilibrium conditions in the vapor,¹ the interpretation of photodissociation spectra,² or thermal desorption.³ Ionization potential measurements also provide interesting but less direct information.⁴ None of these experiments, however, give any insight into the corresponding potential energy surface. A precise determination would be the most direct way to establish the possible existence of isomers (or multiple minima in the potential surface), which is a frequently posed problem in cluster physics. The most valuable test for quantum chemical calculations is obtained from spectroscopic investigations of the ground state. Classical methods like infrared absorption or Raman spectroscopy, however, cannot be applied, because they do not provide size-specific information.

We report in this paper the measurement of Na_3 hot bands, which allowed us to determine the vibrational structure of the electronic ground state. The experimental results are compared

to recent surface potential calculations. Moreover the results enabled us to determine the vibrational temperature of the Na_3 particles in the seeded molecular beam as a function of the stagnation conditions.

Experiment

The crucial part of the experimental setup is the seeded supersonic molecular beam source, which was developed in collaboration with G. D. Stein.^{5,6} Metal vapor is coexpanded into the vacuum with argon as an inert carrier gas by using a very small cylindrical nozzle of 50 μm diameter. The metal vapor pressure inside the oven cartridge ranges between 10 and 100 mbar, while the argon pressure, mainly limited by the 1500 l/s diffusion pump, can reach up to 10 bar. The stagnation conditions provide a strong

(1) Hilpert K., *Ber. Bunsenges. Phys. Chem.* 1984, 88, 260.

(2) (a) Gole, J. L.; Green, G. J.; Pace, S. A.; Preuss, D. R. *J. Chem. Phys.* 1982, 76, 2247. (b) Brucat, B. P. J.; Zheng, L. S.; Pettiette, C. L.; Yang, S.; Smalley, R. E., to be published in *J. Chem. Phys.* (c) Fayet, P.; Wöste, L. *Surf. Sci.* 1985, 156, 134.

(3) Vollmer, M.; Träger, F. "Proceedings of the International Symposium on Metal Cluster (April 1986), Heidelberg, Germany", to be published in *Z. Phys. D*.

(4) (a) Kappes, M. M.; Schär, M.; Radi, P.; Schumacher, E. *J. Chem. Phys.* 1986, 84, 1863, and references therein. (b) Whetten, R. L.; Cox, D. M.; Trevor, D. J.; Kaldor, A. *Surf. Sci.* 1985, 156, 8. (c) Bréchignac, C.; Cahuzac, Ph. *Chem. Phys. Lett.* 1985, 117, 365.

(5) Stein, G.; Delacrétaz, G.; Wöste, L., to be submitted.

(6) Delacrétaz, G. Thesis, 1985, Lausanne, Switzerland.

[†]Université Lyon I.

[‡]Present address: Central Analytical Department, Ciba Geigy Ltd., CH-4002 Basel, Switzerland.

[§]Ecole Polytechnique Federale de Lausanne.